Thermochemical Non-Equilibrium Entry Flows in Mars in Two-Dimensions – Part I

EDISSON SÁVIO DE GÓES MACIEL[(1)] and AMILCAR PORTO PIMENTA[(2)]
IEA – Aeronautical Engineering Division
ITA – Aeronautical Technological Institute
Praça Mal. do Ar Eduardo Gomes, 50 – Vila das Acácias – São José dos Campos – SP – 12228-900
BRAZIL
[(1)]edisavio@edissonsavio.eng.br [(1)]http://www.edissonsavio.eng.br and [(2)]amilcar@ita.br

Abstract: - This work, first part of this study, describes a numerical tool to perform thermochemical non-equilibrium simulations of reactive flow in two-dimensions. The Van Leer and Liou and Steffen Jr. schemes, in their first- and second-order versions, are implemented to accomplish the numerical simulations. The Euler and Navier-Stokes equations, on a finite volume context and employing structured and unstructured spatial discretizations, are applied to solve the "hot gas" hypersonic flows around a blunt body, around a double ellipse, and around an entry capsule, in two-dimensions. The second-order version of the Van Leer and Liou and Steffen Jr. schemes are obtained from a "MUSCL" extrapolation procedure in a context of structured spatial discretization. In the unstructured context, only first-order solutions are obtained. The convergence process is accelerated to the steady state condition through a spatially variable time step procedure, which has proved effective gains in terms of computational acceleration. The reactive simulations involve a Mars atmosphere chemical model of nine species: N, O, N_2, O_2, NO, CO_2, C, CO, and CN, based on the work of Kay and Netterfield. Fifty-three chemical reactions, involving dissociation and recombination, are simulated by the proposed model. The Arrhenius formula is employed to determine the reaction rates and the law of mass action is used to determine the source terms of each gas species equation. The results have indicated the Van Leer TVD scheme as the most accurate one, both inviscid and viscous cases. In this paper is presented the blunt body results. In Part II is presented the results with the double ellipse and the entry capsule.

Key-Words: Thermochemical non-equilibrium, Mars entry, Nine species model, Hypersonic "hot gas" flow, Finite volume, Euler and Navier-Stokes equations, Two-dimensions.

1 Introduction

There has been significant interest in recent years in a mission to Mars. One such proposal is the MARSNET assessment study [1] concerning the potential contribution of ESA (European Space Agency) to a Mars Network mission in cooperation with NASA. NASA is currently studying a network mission MESUR (Mars Environmental Survey), involving the placement of up twenty small scientific stations on the surface of Mars. The objective of the proposed ESA activities is the provision of three of these stations to perform a variety of scientific experiments. The intended entry scenario is an unguided ballistic entry at a typical velocity of 6 km/s using a blunt sphere/cone configuration in which deceleration is provided predominantly by hypersonic aero-braking. It is important that the mass of the vehicle structure and thermal protection system (TPS) be minimized such that the payload delivered to the surface may be maximized.

The trajectory for a ballistic Martian entry takes the vehicle through regions where thermochemical non-equilibrium effects in the surrounding shock layer may be significant. For typical entry velocities (> 5 km/s) the temperature in the shock layer will be sufficiently high for dissociation of the freestream species to occur. The energy removed through such reactions may be released at the vehicle surface via recombination leading to significantly enhanced heat transfer rates. In order to design the TPS for minimum mass the heat transfer rate needs to be accurately predicted. This requires that any catalytic properties of the TPS material are accounted for in the heat transfer rate calculation since these will determine the extent of wall recombination.

As aforementioned, missions to other planets remain an objective for the ESA, and such missions generally involve the entry of a space vehicle into the atmospheres of those planets. In the context of such entry, aerothermodynamics is one of the critical technologies. While the thermochemical behavior of air under re-entry conditions has been studied extensively, and is to some degree understood, the same is not true for entries into other atmospheres. The atmospheres of Mars and

Venus, for example, contain significant amounts of carbon dioxide. In particular, the Mars atmosphere is a mixture of approximately 96% CO_2 and 4% N_2, with pressures much lower than the Earth's atmosphere, so for any entry into the Martian atmosphere the non-equilibrium behavior of CO_2 is likely to be of importance for a typical blunt body entry vehicle. This includes not just the influence of thermochemistry on the forebody heatshield flowfield, but also the influence on the shoulder expansion, base flow, and base heating environment.

Analyzing the reentry flows in Earth, [27] have proposed a numerical tool implemented to simulate inviscid and viscous flows employing the reactive gas formulation of thermal and chemical non-equilibrium. The Euler and Navier-Stokes equations, employing a finite volume formulation, on the context of structured and unstructured spatial discretizations, were solved. These variants allowed an effective comparison between the two types of spatial discretization aiming verify their potentialities: solution quality, convergence speed, computational cost, etc. The aerospace problem involving the hypersonic flow around a blunt body, in two-dimensions, was simulated. The reactive simulations involved an air chemical model of five species: N, O, N_2, O_2 and NO. Seventeen chemical reactions, involving dissociation and recombination, were simulated by the proposed model. The Arrhenius formula was employed to determine the reaction rates and the law of mass action was used to determine the source terms of each gas species equation. Good results were obtained with such code.

This work, first part of this study, describes a numerical tool to perform thermochemical non-equilibrium simulations of reactive flow in two-dimensions. The [2; 22] schemes, in their first- and second-order versions, are implemented to accomplish the numerical simulations. The Euler and Navier-Stokes equations, on a finite volume context and employing structured and unstructured spatial discretizations, are applied to solve the "hot gas" hypersonic flows around a blunt body, around a double ellipse, and around an entry capsule, in two-dimensions. The second-order version of the [2; 22] schemes are obtained from a "MUSCL" extrapolation procedure (details in [3]) in a context of structured spatial discretization. In the unstructured context, only first-order solutions are obtained. The convergence process is accelerated to the steady state condition through a spatially variable time step procedure, which has proved effective gains in terms of computational acceleration (see [4-5]).

The reactive simulations involve a Mars atmosphere chemical model of nine species: N, O, N_2, O_2, NO, CO_2, C, CO, and CN. Fifty-three chemical reactions, involving dissociation and recombination, are simulated by the proposed model. The Arrhenius formula is employed to determine the reaction rates and the law of mass action is used to determine the source terms of each gas species equation.

In this paper only the blunt body solutions are presented. The results have demonstrated that the most correct aerodynamic coefficient of lift in the entry blunt body problem is obtained by the [2] scheme with first-order accuracy, in a viscous formulation, to a reactive condition of thermochemical non-equilibrium. Moreover, the [22] scheme presents the best mass fraction profiles at the stagnation line, characterizing good formation of O and CO. The results obtained with the double ellipse and the entry capsule geometries are presented in [31].

2 Formulation to Reactive Flow in Thermochemical Non-Equilibrium

2.1 Reactive Equations in Two-Dimensions

The reactive Navier-Stokes equations in thermal and chemical non-equilibrium were implemented on a finite volume context, in the two-dimensional space. In this case, these equations in integral and conservative forms can be expressed by:

$$\frac{\partial}{\partial t}\int_V Q dV + \int_S \vec{F}\bullet\vec{n}dS = \int_V S_{CV}dV \text{, with}$$
$$\vec{F} = (E_e - E_v)\vec{i} + (F_e - F_v)\vec{j}, \qquad (1)$$

where: Q is the vector of conserved variables, V is the volume of a computational cell, $\vec{F}$ is the complete flux vector, $\vec{n}$ is the unity vector normal to the flux face, S is the flux area, S_{CV} is the chemical and vibrational source term, E_e and F_e are the convective flux vectors or the Euler flux vectors in the x and y directions, respectively, E_v and F_v are the viscous flux vectors in the x and y directions, respectively. The $\vec{i}$ and $\vec{j}$ unity vectors define the Cartesian coordinate system. Thirteen (13) conservation equations are solved: one of general mass conservation, two of linear momentum conservation, one of total energy, eight of species

mass conservation and one of the vibrational internal energy of the molecules. Therefore, one of the species is absent of the iterative process. The CFD ("Computational Fluid Dynamics") literature recommends that the species of biggest mass fraction of the gaseous mixture should be omitted, aiming to result in a minor numerical accumulation error, corresponding to the biggest mixture constituent (in this case, the Mars atmosphere). To the present study, in which is chosen a chemical model to the Mars atmosphere composed of nine (9) chemical species (N, O, N_2, O_2, NO, CO_2, C, CO, and CN) and fifty-three (53) chemical reactions, this species is the CO_2. The vectors Q, E_e, F_e, E_v, F_v and S_{CV} can, hence, be defined as follows ([6]):

$$Q=\begin{Bmatrix}\rho\\ \rho u\\ \rho v\\ e\\ \rho_1\\ \rho_2\\ \rho_3\\ \rho_4\\ \rho_5\\ \rho_7\\ \rho_8\\ \rho_9\\ \rho e_V\end{Bmatrix},\ E_e=\begin{Bmatrix}\rho u\\ \rho u^2+p\\ \rho uv\\ \rho Hu\\ \rho_1 u\\ \rho_2 u\\ \rho_3 u\\ \rho_4 u\\ \rho_5 u\\ \rho_7 u\\ \rho_8 u\\ \rho_9 u\\ \rho e_V u\end{Bmatrix},\ F_e=\begin{Bmatrix}\rho v\\ \rho vu\\ \rho v^2+p\\ \rho Hv\\ \rho_1 v\\ \rho_2 v\\ \rho_3 v\\ \rho_4 v\\ \rho_5 v\\ \rho_7 v\\ \rho_8 v\\ \rho_9 v\\ \rho e_V v\end{Bmatrix};\quad (2)$$

$$E_v=\frac{1}{Re}\begin{Bmatrix}0\\ \tau_{xx}\\ \tau_{xy}\\ \tau_{xx}u+\tau_{xy}v-q_{f,x}-q_{v,x}-\phi_x\\ -\rho_1 v_{1x}\\ -\rho_2 v_{2x}\\ -\rho_3 v_{3x}\\ -\rho_4 v_{4x}\\ -\rho_5 v_{5x}\\ -\rho_7 v_{7x}\\ -\rho_8 v_{8x}\\ -\rho_9 v_{9x}\\ -q_{v,x}-\phi_{v,x}\end{Bmatrix};\quad (3)$$

in which: ρ is the mixture density; u and v are Cartesian components of the velocity vector in the x and y directions, respectively; p is the fluid static pressure; e is the fluid total energy; ρ_1, ρ_2, ρ_3, ρ_4, ρ_5, ρ_7, ρ_8, and ρ_9 are densities of the N, O, N_2, O_2, NO, C, CO and CN, respectively;

$$F_v=\frac{1}{Re}\begin{Bmatrix}0\\ \tau_{xy}\\ \tau_{yy}\\ \tau_{xy}u+\tau_{yy}v-q_{f,y}-q_{v,y}-\phi_y\\ -\rho_1 v_{1y}\\ -\rho_2 v_{2y}\\ -\rho_3 v_{3y}\\ -\rho_4 v_{4y}\\ -\rho_5 v_{5y}\\ -\rho_7 v_{7y}\\ -\rho_8 v_{8y}\\ -\rho_9 v_{9y}\\ -q_{v,y}-\phi_{v,y}\end{Bmatrix},\quad (4)$$

$$S_{CV}=\begin{Bmatrix}0\\ 0\\ 0\\ 0\\ \dot{\omega}_1\\ \dot{\omega}_2\\ \dot{\omega}_3\\ \dot{\omega}_4\\ \dot{\omega}_5\\ \dot{\omega}_7\\ \dot{\omega}_8\\ \dot{\omega}_9\\ \sum_{s=mol}\rho_s\left(e^*_{v,s}-e_{v,s}\right)/\tau_s+\sum_{s=mol}\dot{\omega}_s e_{v,s}\end{Bmatrix},\quad (5)$$

H is the mixture total enthalpy; e_V is the sum of the vibrational energy of the molecules; the τ's are the components of the viscous stress tensor; $q_{f,x}$ and $q_{f,y}$ are the frozen components of the Fourier-heat-flux vector in the x and y directions, respectively; $q_{v,x}$ and $q_{v,y}$ are the components of the Fourier-heat-flux vector calculated with the vibrational thermal conductivity and vibrational temperature; $\rho_s v_{sx}$ and $\rho_s v_{sy}$ represent the species diffusion flux, defined by the Fick law; ϕ_x and ϕ_y are the terms of mixture diffusion; $\phi_{v,x}$ and $\phi_{v,y}$ are the terms of molecular diffusion calculated at the vibrational temperature; $\dot{\omega}_s$ is the chemical source term of each species

equation, defined by the law of mass action; e_v^* is the molecular-vibrational-internal energy calculated with the translational/rotational temperature; and τ_s is the translational-vibrational characteristic relaxation time of each molecule.

The viscous stresses, in N/m^2, are determined, according to a Newtonian fluid model, by:

$$\tau_{xx} = 2\mu\frac{\partial u}{\partial x} - \frac{2}{3}\mu\left(\frac{\partial u}{\partial x} + \frac{\partial v}{\partial y}\right),$$

$$\tau_{xy} = \mu\left(\frac{\partial u}{\partial y} + \frac{\partial v}{\partial x}\right) \text{ and } \tau_{yy} = 2\mu\frac{\partial v}{\partial y} - \frac{2}{3}\mu\left(\frac{\partial u}{\partial x} + \frac{\partial v}{\partial y}\right), \quad (6)$$

in which μ is the fluid molecular viscosity.

The frozen components of the Fourier-heat-flux vector, which considers only thermal conduction, are defined by:

$$q_{f,x} = -k_f\frac{\partial T}{\partial x} \quad \text{and} \quad q_{f,y} = -k_f\frac{\partial T}{\partial y}, \quad (7)$$

where k_f is the mixture frozen thermal conductivity, calculated conform presented in section **2.3.** The vibrational components of the Fourier-heat-flux vector are calculated as follows:

$$q_{v,x} = -k_v\frac{\partial T_v}{\partial x} \quad \text{and} \quad q_{v,y} = -k_v\frac{\partial T_v}{\partial y}, \quad (8)$$

in which k_v is the vibrational thermal conductivity and T_v is the vibrational temperature, what characterizes this model as of two temperatures: translational/rotational and vibrational. The calculation of T_v and k_v are presented in section **2.3**.

The terms of species diffusion, defined by the Fick law, to a condition of thermal non-equilibrium, are determined by ([6]):

$$\rho_s v_{sx} = -\rho D_s\frac{\partial Y_{MF,s}}{\partial x} \quad \text{and} \quad \rho_s v_{sy} = -\rho D_s\frac{\partial Y_{MF,s}}{\partial y}, \quad (9)$$

with "s" referent to a given species, $Y_{MF,s}$ being the molar fraction of the species, defined as:

$$Y_{MF,s} = \frac{\rho_s / M_s}{\sum_{k=1}^{ns}\rho_k / M_k} \quad (10)$$

and D_s is the species-effective-diffusion coefficient.

The diffusion terms ϕ_x and ϕ_y which appear in the energy equation are defined by ([7]):

$$\phi_x = \sum_{s=1}^{ns}\rho_s v_{sx} h_s \quad \text{and} \quad \phi_y = \sum_{s=1}^{ns}\rho_s v_{sy} h_s, \quad (11)$$

being h_s the specific enthalpy (sensible) of the chemical species "s". The specific enthalpy is calculated as function of the several modes of internal energy as follows:

$$e_{i,trans} = 3/2 R_s T;$$

$$e_{i,rot} = \begin{cases} 0, & \text{atoms} \\ R_s T, & \text{molecules} \end{cases};$$

$$e_{i,vib} = \begin{cases} 0, & \text{atoms} \\ \dfrac{R_s\theta_{v,s}}{e^{\theta_{v,s}/T_v} - 1}, & \text{molecules} \end{cases};$$

$$e_{i,0} = \Delta h_{f,s} - R_s T_{ref};$$

$$e_i = e_{i,trans} + e_{i,rot} + e_{i,vib} + e_{i,0};$$

$$h_s = e_i + R_s T. \quad (12)$$

The molecular diffusion terms calculated at the vibrational temperature, $\phi_{v,x}$ and $\phi_{v,y}$, which appear in the vibrational-internal-energy equation are defined by ([6]):

$$\phi_{v,x} = \sum_{s=mol}\rho_s v_{sx} h_{v,s} \text{ and } \phi_{v,y} = \sum_{s=mol}\rho_s v_{sy} h_{v,s}, \quad (13)$$

with $h_{v,s}$ being the specific enthalpy (sensible) of the chemical species "s" calculated at the vibrational temperature T_v. The sum of Eq. (13), as also those present in Eq. (5), considers only the molecules of the system, namely: N_2, O_2, NO, CO_2, CO and CN.

Table 1. Molecular mass and enthalpy formation of each species.

Species	M (g/g-mol)	$\Delta h_{f,s}$ (J/g-mol)
N	14.0	472,680.0
O	16.0	249,180.0
N_2	28.0	0.0
O_2	32.0	0.0
NO	30.0	90,290.0
CO_2	44.0	-393,510.0
C	12.0	716,680.0
CO	28.0	-110,530.0
CN	26.0	435,100.0

The molecular mass and the formation enthalpy of each constituent of the Mars atmosphere are

given in Tab. 1. Note that to have $\Delta h_{f,s}$ in J/kg, it is only necessary to multiply it by 10^3 and to divide it by the molecular mass.

2.2 Chemical Model and Reaction Data

The following species are considered for entry into the Martian atmosphere:

N, O, N_2, O_2, NO, CO_2, C, CO, and CN.

These species represent the main constituents of a high temperature mixture of carbon dioxide and nitrogen. The CN molecule is included for assessment purposes though is not expected to be present in large mass fractions. For the moderate entry velocities considered in this work ionization is assumed to be unimportant, thus no ionic species are considered. This chemical model is based on the work of [29]. The reaction set used for these calculations is given in Tab. 2. Reverse reaction rate data are specified directly in Tab. 3. It is assumed that both the forward and reverse reaction rate coefficients have the following Arrhenius temperature dependence:

$$k = AT^{\beta} e^{-C/T}, \qquad (14)$$

where the pre-exponential factor A, the temperature exponent β and the activation energy C are obtained from experiment and are given in Tabs. 2 and 3. M is a third body of collision and can be any species. Data for the forward reactions 1 to 4 and 6 to 10 are taken from [8].

Table 2. Reactions and forward coefficients.

Reaction	A	β	C
O_2+M ↔ O+O+M	$9.1\text{x}10^{18}$	-1.0	59370
N_2+M ↔ N+N+M	$2.5\text{x}10^{19}$	-1.0	113200
NO+M ↔ N+O+M	$4.1\text{x}10^{18}$	-1.0	75330
CO+M ↔ C+O+M	$4.5\text{x}10^{19}$	-1.0	128900
CO_2+M ↔ CO+O+M	$3.7\text{x}10^{14}$	0.0	52500
N_2+O ↔ NO+N	$7.4\text{x}10^{11}$	0.5	37940
NO+O ↔ O_2+N	$3.0\text{x}10^{11}$	0.5	19460
CO+O ↔ C+O_2	$2.7\text{x}10^{12}$	0.5	69540
CO_2+O ↔ CO+O_2	$1.7\text{x}10^{13}$	0.0	26500
CO+N ↔ NO+C	$2.9\text{x}10^{11}$	0.5	53630
CN+O ↔ NO+C	$1.6\text{x}10^{13}$	0.1	14600
CO+N ↔ CN+O	$2.0\text{x}10^{14}$	0.0	38600
N_2+C ↔ CN+N	$2.0\text{x}10^{14}$	0.0	23200

Reaction 5 and 11 to 13 are taken from [9]. Data for the reverse reactions are taken from [8], except for reactions 5 and 9 for which data are from reference [10], and reactions 11 to 13 where data are from [11]. For dissociation reactions the preferential model of Park is used whereby the forward rates are governed by an average temperature $T_a = \sqrt{T.T_v}$. With all combinations to M, a total of fifth-three (53) reactions are obtained.

Table 3. Reactions and reverse coefficients.

Reaction	A	β	C
O_2+M ↔ O+O+M	$9.0\text{x}10^{15}$	-0.5	0.0
N_2+M ↔ N+N+M	$1.5\text{x}10^{18}$	-1.0	0.0
NO+M ↔ N+O+M	$3.5\text{x}10^{18}$	-1.0	0.0
CO+M ↔ C+O+M	$1.0\text{x}10^{18}$	-1.0	0.0
CO_2+M ↔ CO+O+M	$2.4\text{x}10^{15}$	0.0	2184
N_2+O ↔ NO+N	$1.6\text{x}10^{11}$	0.5	0.0
NO+O ↔ O_2+N	$9.5\text{x}10^{09}$	1.0	0.0
CO+O ↔ C+O_2	$9.4\text{x}10^{12}$	0.25	0.0
CO_2+O ↔ CO+O_2	$2.5\text{x}10^{12}$	0.0	24000
CO+N ↔ NO+C	$2.6\text{x}10^{10}$	0.5	0.0
CN+O ↔ NO+C	$3.8\text{x}10^{12}$	0.5	4500
CO+N ↔ CN+O	$6.3\text{x}10^{11}$	0.5	4500
N_2+C ↔ CN+N	$4.4\text{x}10^{14}$	0.0	4500

2.3 Transport Properties

For species N, O, N_2, O_2 and NO curve fits for viscosity as a function of temperature have been developed by [12] which are of the form

$$\mu = 0.1 \times \exp\left[\left(A_\mu \ln T + B_\mu\right)\ln T + C_\mu\right]. \qquad (15)$$

[13] develops equivalent curve fits for CO and CO_2, while C is assumed to behave as O. For CN data are from [14]. Data for these curve fits are given in Tab. 4.

Table 4. Coefficients for viscosity curve fits.

Species	A_μ	B_μ	C_μ
N	0.0115572	0.4294404	-12.4327495
O	0.0203144	0.4294404	-11.6031403
N_2	0.0268142	0.3177838	-11.3155513
O_2	0.0449290	-0.0826158	-9.2019475
NO	0.0436378	-0.0335511	-9.5767430
CO_2	-0.0195274	1.0132950	-13.9787300
C	0.0203144	0.4294404	-11.6031403
CO	-0.0195274	1.0478180	-14.3221200
CN	-0.0025000	0.6810000	-12.4914000

The thermal conductivity of translational and rotational energies for each species is derived from species viscosities using an Eucken relation:

$$k_{tr,i} = \left(5/2 \times c_{v,t,i} + c_{v,r,i}\right), \quad (16)$$

where:

$$c_{v,t} = \begin{cases} 3/2RT, & \text{for molecules} \\ 0.0, & \text{for atoms.} \end{cases} \quad (17)$$
$$c_{v,r} = RT$$

The total viscosity and conductivity of the gas mixture are calculated using the semi-empirical rule of [15]. To the viscosity, for instance:

$$\mu = \sum_{i=1}^{ns} \frac{X_i \mu_i}{\phi_i}, \quad (18)$$

where X_i is the mole fraction of species i and

$$\phi_i = \sum_{j=1}^{ns} \frac{X_j \left[1 + \sqrt{\frac{\mu_i}{\mu_j}} \left(\frac{M_j}{M_i}\right)^{1/4}\right]^2}{\sqrt{8\left(1 + \frac{M_i}{M_j}\right)}}. \quad (19)$$

X_i can be calculated from

$$X_i = \frac{c_i M}{M_i}, \quad (20)$$

with:

$$M = 1 \Big/ \sum_{j=1}^{ns} \frac{c_j}{M_j}; \quad (21)$$

$$c_j = \frac{\rho_j}{\rho} \text{ (Mass fraction).} \quad (22)$$

Diffusion coefficients are computed as outlined by [16]. The species diffusion coefficients are calculated from

$$D_i = \frac{\frac{M_i}{M}(1 - c_i)D}{1 - X_i}. \quad (23)$$

The diffusion coefficient D is calculated from the Schmidt number:

$$S_c = \frac{\mu}{\rho D}. \quad (24)$$

The Schmidt number is set to 0.5 for neutral species and 0.25 for ions.

The species vibrational conductivities are also calculated by the species viscosity and the Eucken formula:

$$k_{v,i} = \mu_i R_i. \quad (25)$$

The vibrational temperature is determined from the definition of the internal vibrational energy of the mixture, on an iterative process, and uses the Newton-Raphson method to find the root, which is merely the approximate vibrational temperature. Three steps are suffice to obtain a good approximation.

2.4 Source Terms

The source terms for the species mass fractions in the chemically reacting flow are giving by:

$$\dot{\omega}_i = M_i \sum_{r=1}^{nr} \left(\nu''_{i,r} - \nu'_{i,r}\right) \times \left\{ k_{f,i} \prod_{j=1}^{jmax} \left(\rho_j / M_j\right)^{\nu'_{j,r}} - k_{r,i} \prod_{j=1}^{jmax} \left(\rho_j / M_j\right)^{\nu''_{j,r}} \right\}. \quad (26)$$

The reaction rate coefficients k_f and k_r are calculated as a function of a rate controlling temperature T_a, as given in section **2.2**.

2.5 Vibrational Relaxation Model

The vibrational internal energy of a molecule, in J/kg, is defined by:

$$e_{v,s} = \frac{R_s \theta_{v,s}}{e^{\theta_{V,s}/T_V} - 1}, \quad (27)$$

and the vibrational internal energy of all molecules is given by:

$$e_V = \sum_{s=mol} c_s e_{v,s}. \quad (28)$$

The heat flux due to translational-vibrational relaxation, according to [17], is given by:

$$q_{T-V,s} = \rho_s \frac{e^*_{v,s}(T) - e_{v,s}(T_v)}{\tau_s}, \qquad (29)$$

where: $e^*_{v,s}$ is the vibrational internal energy calculated at the translational temperature to the species "s"; and τ_s is the translational-vibrational relaxation time to the molecular species, in s. The relaxation time is the time of energy exchange between the translational and vibrational molecular modes.

2.5.1 Vibrational characteristic time of [18]

According to [18], the relaxation time of molar average of [19] is described by:

$$\tau_s = \tau_s^{M-W} = \sum_{l=1}^{ns} X_l \Big/ \sum_{l=1}^{ns} X_l / \tau_{s,l}^{M-W}, \qquad (30)$$

with:

$\tau_{s,l}^{M-W}$ is the relaxation time between species of [19];

τ_s^{M-W} is the vibrational characteristic time of [19];

$$X_l = c_l / (N_{AV} m_l) \text{ and } m_l = M_l / N_{AV}. \qquad (31)$$

2.5.2 Definition of $\tau_{s,l}^{M-W}$:

For temperatures inferior to or equal to 8,000 K, [19] give the following semi-empirical correlation to the vibrational relaxation time due to inelastic collisions:

$$\tau_{s,l}^{M-W} = \left(\frac{B}{p_l}\right) e^{\left[A_{s,l}\left(T^{-1/3} - 0.015\mu_{s,l}^{1/4}\right) - 18.42\right]}, \qquad (32)$$

where:

$B = 1.013 \times 10^5 Ns/m^2$ ([20]);

p_l is the partial pressure of species "l" in N/m^2;

$$A_{s,l} = 1.16 \times 10^{-3} \mu_{s,l}^{1/2} \theta_{v,s}^{4/3} \text{ ([20])}; \qquad (33)$$

$$\mu_{s,l} = \frac{M_s M_l}{M_s + M_l}, \qquad (34)$$

being the reduced molecular mass of the collision partners: kg/kg-mol;

T and $\theta_{v,s}$ in Kelvin.

The values of the characteristic vibrational temperature are given in Tab. 5. In the absence of specific vibrational relaxation data for CN the molecule has been assumed to behave as CO.

Table 5. Vibrational energy constants.

Species	θ_v (K)
N_2	3395.0
O_2	2239.0
NO	2817.0
CO	3074.0
CN	3074.0

2.5.3 [21] correction time

For temperatures superiors to 8,000 K, the Eq. (32) gives relaxation times less than those observed in experiments. To temperatures above 8,000 K, [21] suggests the following relation to the vibrational relaxation time:

$$\tau_s^P = \frac{1}{\xi_s \sigma_v n_s}, \qquad (35)$$

where:

$$\xi_s = \sqrt{\frac{8R_s T}{\pi}}, \qquad (36)$$

being the molecular average velocity in m/s;

$$\sigma_v = 10^{-20}\left(\frac{50{,}000}{T}\right)^2, \qquad (37)$$

being the effective collision cross-section to vibrational relaxation in m^2; and

$$n_s = \rho_s / m_s, \qquad (38)$$

being the density of the number of collision particles of species "s". ρ_s in kg/m^3 and m_s in kg/particle, defined by Eq. (31).

Combining the two relations, the following expression to the vibrational relaxation time is obtained:

$$\tau_s = \tau_s^{M-W} + \tau_s^P. \qquad (39)$$

[21] emphasizes that this expression [Eq. (39)] to the vibrational relaxation time is applicable to a range of temperatures much more vast.

3 Structured Van Leer and Liou and Steffen Jr. Algorithms to Thermochemical Non-Equilibrium

The approximation of the integral equation (1) to a rectangular finite volume yields a system of ordinary differential equations with respect to time:

$$V_{i,j}\, dQ_{i,j}/dt = -C_{i,j}, \tag{40}$$

with $C_{i,j}$ representing the net flux (residue) of conservation of mass, of linear momentum, of total energy, of species mass conservation, and of vibrational energy in the $V_{i,j}$ volume. The cell volume is defined by:

$$V_{i,j} = 0.5\left|\left(x_{i,j}-x_{i+1,j}\right)y_{i+1,j+1}+\left(x_{i+1,j}-x_{i+1,j+1}\right)y_{i,j}+\left(x_{i+1,j+1}-x_{i,j}\right)y_{i+1,j}\right| + 0.5\left|\left(x_{i,j}-x_{i+1,j+1}\right)y_{i,j+1}+\left(x_{i+1,j+1}-x_{i,j+1}\right)y_{i,j}+\left(x_{i,j+1}-x_{i,j}\right)y_{i+1,j+1}\right|, \tag{41}$$

where a computational cell and its flux surfaces are defined in Fig. 1.

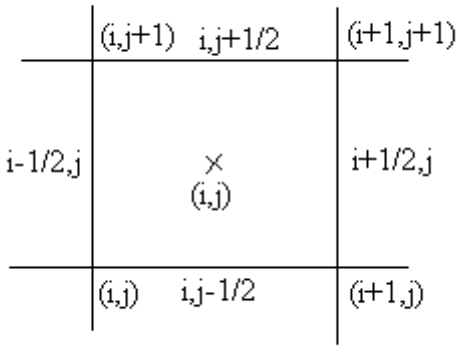

Figure 1. Structured computational cell.

As shown in [22], the discrete convective flux calculated by the AUSM scheme ("Advection Upstream Splitting Method") can be interpreted as a sum involving the arithmetical average between the right (R) and the left (L) states of the (i+1/2,j) cell face, related to cell (i,j) and its (i+1,j) neighbour, respectively, multiplied by the interface Mach number, and a scalar dissipative term. Hence, to the (i+1/2,j) interface, considering the dynamical part of the formulation:

$$R_{i+1/2,j} = |S|_{i+1/2,j}\left\{\frac{1}{2}M_{i+1/2,j}\left[\begin{pmatrix}\rho a\\ \rho a u\\ \rho a v\\ \rho a H\end{pmatrix}_L+\begin{pmatrix}\rho a\\ \rho a u\\ \rho a v\\ \rho a H\end{pmatrix}_R\right] - \frac{1}{2}\phi_{i+1/2,j}\left[\begin{pmatrix}\rho a\\ \rho a u\\ \rho a v\\ \rho a H\end{pmatrix}_R-\begin{pmatrix}\rho a\\ \rho a u\\ \rho a v\\ \rho a H\end{pmatrix}_L\right]\right\}+\begin{pmatrix}0\\ S_x p\\ S_y p\\ 0\end{pmatrix}_{i+1/2,j}. \tag{42}$$

The components of the unity vector normal to the flux interface and the area of the flux interface "l", n_x^l, n_y^l and S^l, are defined as:

$$n_x^l = \Delta y_l/\left(\Delta x_l^2+\Delta y_l^2\right)^{0.5},$$
$$n_y^l = -\Delta x_l/\left(\Delta x_l^2+\Delta y_l^2\right)^{0.5},$$
$$S^l = \left(\Delta x_l^2+\Delta y_l^2\right)^{0.5}. \tag{43}$$

Expressions to Δx_l and Δy_l are given in Tab. 6. The area components are obtained by the product of the respective normal vector component and the area S.

Table 6. Values of Δx_l and Δy_l to the structured case.

Interface	Δx_l	Δy_l
l = (i,j-1/2)	$x_{i+1,j}-x_{i,j}$	$y_{i+1,j}-y_{i,j}$
l = (i+1/2,j)	$x_{i+1,j+1}-x_{i+1,j}$	$y_{i+1,j+1}-y_{i+1,j}$
l = (i,j+1/2)	$x_{i,j+1}-x_{i+1,j+1}$	$y_{i,j+1}-y_{i+1,j+1}$
l = (i-1/2,j)	$x_{i,j}-x_{i,j+1}$	$y_{i,j}-y_{i,j+1}$

The "a" quantity represents the frozen speed of sound. $M_{i+1/2,j}$ defines the advection Mach number at the (i+1/2,j) face of the (i,j) cell, which is calculated according to [22] as:

$$M_l = M_L^+ + M_R^-, \tag{44}$$

where the separated Mach numbers $M^{+/-}$ are defined by the [2] formulas:

$$M^+ = \begin{cases} M, & \text{if } M \ge 1;\\ 0.25(M+1)^2, & \text{if } |M|<1;\\ 0, & \text{if } M \le -1;\end{cases} \tag{45a}$$

$$M^{-}=\begin{cases}0, & \text{if } M\geq 1;\\ -0.25(M-1)^2, & \text{if } |M|<1;\\ M, & \text{if } M\leq -1.\end{cases} \quad (45b)$$

M_L and M_R represent the Mach number associated with the left and right states, respectively. The advection Mach number is defined by:

$$M=\left(S_x u+S_y v\right)/\left(|S|a\right). \quad (46)$$

The pressure at the (i+1/2,j) face of the (i,j) cell is calculated by a similar way:

$$p_l=p_L^{+}+p_R^{-}, \quad (47)$$

with $p^{+/-}$ denoting the pressure separation defined according to the [2] formulas:

$$p^{+}=\begin{cases}p, & \text{if } M\geq 1;\\ 0.25p(M+1)^2(2-M), & \text{if } |M|<1;\\ 0, & \text{if } M\leq -1;\end{cases}$$
$$p^{-}=\begin{cases}0, & \text{if } M\geq 1;\\ 0.25p(M-1)^2(2+M), & \text{if } |M|<1;\\ p, & \text{if } M\leq -1.\end{cases} \quad (48)$$

The definition of the dissipative term ϕ determines the particular formulation of the convective fluxes. According to [23], the choice below corresponds to the [2] scheme:

$$\phi_{i+1/2,j}=\begin{cases}|M_{i+1/2,j}|, & \text{if } |M_{i+1/2,j}|\geq 1;\\ |M_{i+1/2,j}|+0.5(M_R-1)^2, & \text{if } 0\leq M_{i+1/2,j}<1;\\ |M_{i+1/2,j}|+0.5(M_L+1)^2, & \text{if } -1<M_{i+1/2,j}\leq 0;\end{cases} \quad (49)$$

and the choice below corresponds to the [22] scheme:

$$\phi_{i+1/2,j}=|M_{i+1/2,j}|; \quad (50)$$

the discrete-chemical-convective flux is defined by:

$$R_{i+1/2,j}=|S|_{i+1/2,j}\left\{\frac{1}{2}M_{i+1/2,j}\left[\begin{pmatrix}\rho_1 a\\ \rho_2 a\\ \rho_3 a\\ \rho_4 a\\ \rho_5 a\\ \rho_7 a\\ \rho_8 a\\ \rho_9 a\end{pmatrix}_L+\begin{pmatrix}\rho_1 a\\ \rho_2 a\\ \rho_3 a\\ \rho_4 a\\ \rho_5 a\\ \rho_7 a\\ \rho_8 a\\ \rho_9 a\end{pmatrix}_R\right]\right.$$
$$\left.-\frac{1}{2}\phi_{i+1/2,j}\left[\begin{pmatrix}\rho_1 a\\ \rho_2 a\\ \rho_3 a\\ \rho_4 a\\ \rho_5 a\\ \rho_7 a\\ \rho_8 a\\ \rho_9 a\end{pmatrix}_R-\begin{pmatrix}\rho_1 a\\ \rho_2 a\\ \rho_3 a\\ \rho_4 a\\ \rho_5 a\\ \rho_7 a\\ \rho_8 a\\ \rho_9 a\end{pmatrix}_L\right]\right\}, \quad (51)$$

and the discrete-vibrational-convective flux is determined by:

$$R_{i+1/2,j}=|S|_{i+1/2,j}\left\{\frac{1}{2}M_{i+1/2,j}\left[(\rho e_v a)_L+(\rho e_v a)_R\right]\right.$$
$$\left.-\frac{1}{2}\phi_{i+1/2,j}\left[(\rho e_v a)_R-(\rho e_v a)_L\right]\right. \quad (52)$$

The time integration is performed employing the Runge-Kutta explicit method of five stages, second-order accurate, to the three types of convective flux.

To the dynamic part, this method can be represented in general form by:

$$\begin{aligned}Q_{i,j}^{(0)}&=Q_{i,j}^{(n)}\\ Q_{i,j}^{(k)}&=Q_{i,j}^{(0)}-\alpha_k\Delta t_{i,j}\,R\left(Q_{i,j}^{(k-1)}\right)/V_{i,j},\\ Q_{i,j}^{(n+1)}&=Q_{i,j}^{(k)}\end{aligned} \quad (53)$$

to the chemical part, it can be represented in general form by:

$$\begin{aligned}Q_{i,j}^{(0)}&=Q_{i,j}^{(n)}\\ Q_{i,j}^{(k)}&=Q_{i,j}^{(0)}-\alpha_k\Delta t_{i,j}\left[R\left(Q_{i,j}^{(k-1)}\right)/V_{i,j}-S_C\left(Q_{i,j}^{(k-1)}\right)\right],\\ Q_{i,j}^{(n+1)}&=Q_{i,j}^{(k)}\end{aligned} \quad (54)$$

where the chemical source term S_C is calculated with the temperature T_a. Finally, to the vibrational part:

$$\begin{aligned} Q_{i,j}^{(0)} &= Q_{i,j}^{(n)} \\ Q_{i,j}^{(k)} &= Q_{i,j}^{(0)} - \alpha_k \Delta t_{i,j}\left[R\left(Q_{i,j}^{(k-1)}\right)/V_{i,j} - S_v\left(Q_{i,j}^{(k-1)}\right)\right], \\ Q_{i,j}^{(n+1)} &= Q_{i,j}^{(k)} \end{aligned} \tag{55}$$

in which:

$$S_v = \sum_{s=mol} q_{T-V,s} + \sum_{s=mol} S_{C,s} e_{v,s}\ ; \tag{56}$$

k = 1,...,5; $\alpha_1 = 1/4$, $\alpha_2 = 1/6$, $\alpha_3 = 3/8$, $\alpha_4 = 1/2$ and $\alpha_5 = 1$. This scheme is first-order accurate in space and second-order accurate in time. The second-order of spatial accuracy is obtained by the "MUSCL" procedure.

The viscous formulation follows that of [24], which adopts the Green theorem to calculate primitive variable gradients. The viscous vectors are obtained by arithmetical average between cell (i,j) and its neighbours. As was done with the convective terms, there is a need to separate the viscous flux in three parts: dynamical viscous flux, chemical viscous flux and vibrational viscous flux. The dynamical part corresponds to the first four equations of the Navier-Stokes ones, the chemical part corresponds to the following eight equations and the vibrational part corresponds to the last equation.

4 MUSCL Procedure

Second order spatial accuracy can be achieved by introducing more upwind points or cells in the schemes. It has been noted that the projection stage, whereby the solution is projected in each cell face (i-1/2,j; i+1/2,j) on piecewise constant states, is the cause of the first order space accuracy of the Godunov schemes ([3]). Hence, it is sufficient to modify the first projection stage without modifying the Riemann solver, in order to generate higher spatial approximations. The state variables at the interfaces are thereby obtained from an extrapolation between neighboring cell averages. This method for the generation of second order upwind schemes based on variable extrapolation is often referred to in the literature as the MUSCL approach. The use of nonlinear limiters in such procedure, with the intention of restricting the amplitude of the gradients appearing in the solution, avoiding thus the formation of new extrema, allows that first order upwind schemes be transformed in TVD high resolution schemes with the appropriate definition of such nonlinear limiters, assuring monotone preserving and total variation diminishing methods. Details of the present implementation of the MUSCL procedure, as well the incorporation of TVD properties to the schemes, are found in [3]. The expressions to calculate the fluxes following a MUSCL procedure and the nonlinear flux limiter definitions employed in this work, which incorporates TVD properties, are defined as follows.

The conserved variables at the interface (i+1/2,j) can be considered as resulting from a combination of backward and forward extrapolations. To a linear one-sided extrapolation at the interface between the averaged values at the two upstream cells (i,j) and (i-1,j), one has:

$$Q_{i+1/2,j}^{L} = Q_{i,j} + \frac{\varepsilon}{2}\left(Q_{i,j} - Q_{i-1,j}\right), \text{ cell (i,j)}; \tag{57}$$

$$Q_{i+1/2,j}^{R} = Q_{i+1,j} - \frac{\varepsilon}{2}\left(Q_{i+2,j} - Q_{i+1,j}\right), \text{ cell (i+1,j)}, \tag{58}$$

leading to a second order fully one-sided scheme. If the first order scheme is defined by the numerical flux

$$F_{i+1/2,j} = F\left(Q_{i,j}, Q_{i+1,j}\right) \tag{59}$$

the second order space accurate numerical flux is obtained from

$$F_{i+1/2,j}^{(2)} = F\left(Q_{i+1/2,j}^{L}, Q_{i+1/2,j}^{R}\right). \tag{60}$$

Higher order flux vector splitting methods, such as those studied in this work, are obtained from:

$$F_{i+1/2,j}^{(2)} = F^{+}\left(Q_{i+1/2,j}^{L}\right) + F^{-}\left(Q_{i+1/2,j}^{R}\right). \tag{61}$$

All second order upwind schemes necessarily involve at least five mesh points or cells.

To reach high order solutions without oscillations around discontinuities, nonlinear limiters are employed, replacing the term ε in Eqs. (57) and (58) by these limiters evaluated at the left and at the right states of the flux interface. To define such limiters, it is necessary to calculate the ratio of consecutive variations of the conserved variables. These ratios are defined as follows:

$$r_{i-1/2,j}^{+} = \left(Q_{i+1,j} - Q_{i,j}\right)/\left(Q_{i,j} - Q_{i-1,j}\right) \tag{62a}$$

$$r^{+}_{i+1/2,j} = \left(Q_{i+2,j} - Q_{i+1j}\right) / \left(Q_{i+1,j} - Q_{i,j}\right), \quad (62b)$$

where the nonlinear limiters at the left and at the right states of the flux interface are defined by $\Psi^{L} = \Psi\left(r^{+}_{i-1/2,j}\right)$ and $\Psi^{R} = \Psi\left(1/r^{+}_{i+1/2,j}\right)$. In this work, five options of nonlinear limiters were considered to the numerical experiments. These limiters are defined as follows:

$$\Psi_l^{VL}(r_l) = \frac{r_l + |r_l|}{1 + r_l}, \text{ [25] limiter;} \quad (63)$$

$$\Psi_l^{VA}(r_l) = \frac{r_l + r_l^2}{1 + r_l^2}, \text{ Van Albada limiter;} \quad (64)$$

$$\Psi_l^{MIN}(r_l) = signal_l MAX\left(0, MIN\left(|r_l|, signal_l\right)\right), \text{ minmod limiter;} \quad (65)$$

$$\Psi_l^{SB}(r_l) = MAX\left(0, MIN(2r_l, 1), MIN(r_l, 2)\right), \text{ “Super Bee” limiter, due to [26];} \quad (66)$$

$$\Psi_l^{\beta-L}(r_l) = MAX\left(0, MIN(\beta r_l, 1), MIN(r_l, \beta)\right), \quad \beta\text{-limiter,} \quad (67)$$

with “l” varying from 1 to 13 (two-dimensional space), $signal_l$ being equal to 1.0 if $r_l \geq 0.0$ and -1.0 otherwise, r_l is the ratio of consecutive variations of the lth conserved variable and β is a parameter assuming values between 1.0 and 2.0, being 1.5 the value assumed in this work.

With the implementation of the numerical flux vectors following this MUSCL procedure, second order spatial accuracy and TVD properties are incorporated in the algorithms.

5 Unstructured Van Leer and Liou and Steffen Jr. Algorithms to Thermochemical Non-Equilibrium

The cell volume on an unstructured context is defined by:

$$V_i = 0.5\left|\left(x_{n1}y_{n2} + y_{n1}x_{n3} + x_{n2}y_{n3}\right) - \left(x_{n3}y_{n2} + y_{n3}x_{n1} + x_{n2}y_{n1}\right)\right|, \quad (68)$$

with n_1, n_2 and n_3 being the nodes of a given triangular cell. The description of the computational cell and its nodes, flux interfaces and neighbors are shown in Fig. 2.

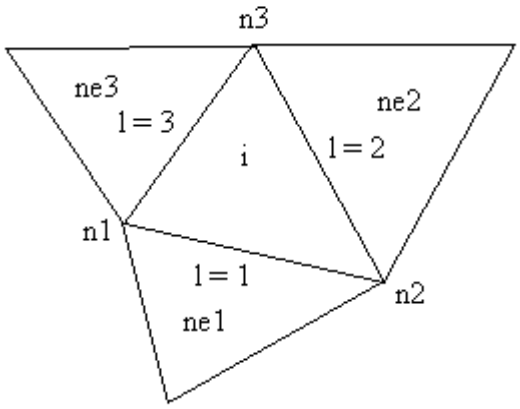

Figure 2. Schematic of a cell and its neighbours, nodes and flux interfaces.

The area components at the “l” interface are defined by:

$$S_x^l = n_x^l S^l \quad \text{and} \quad S_y^l = n_y^l S^l, \quad (69)$$

where n_x^l, n_y^l and S^l are defined as:

$$n_x^l = \Delta y_l / \left(\Delta x_l^2 + \Delta y_l^2\right)^{0.5}, \; n_y^l = -\Delta x_l / \left(\Delta x_l^2 + \Delta y_l^2\right)^{0.5}; \quad S^l = \left(\Delta x_l^2 + \Delta y_l^2\right)^{0.5}. \quad (70)$$

Expressions to Δx_l and Δy_l are given in Tab. 7.

Table 7. Values of Δx_l and Δy_l.

Interface	Δx_l	Δy_l
l = 1	$x_{n2} - x_{n1}$	$y_{n2} - y_{n1}$
l = 2	$x_{n3} - x_{n2}$	$y_{n3} - y_{n2}$
l = 3	$x_{n1} - x_{n3}$	$y_{n1} - y_{n3}$

Considering the two-dimensional and unstructured case, the algorithm follows that described in section **3**. Hence, the discrete-dynamic-convective flux is defined by:

$$R_1 = |S|_1 \left\{ \frac{1}{2} M_1 \left[\begin{pmatrix} \rho a \\ \rho a u \\ \rho a v \\ \rho a H \end{pmatrix}_L + \begin{pmatrix} \rho a \\ \rho a u \\ \rho a v \\ \rho a H \end{pmatrix}_R \right] - \frac{1}{2} \phi_1 \left[\begin{pmatrix} \rho a \\ \rho a u \\ \rho a v \\ \rho a H \end{pmatrix}_R - \begin{pmatrix} \rho a \\ \rho a u \\ \rho a v \\ \rho a H \end{pmatrix}_L \right] \right\} + \begin{pmatrix} 0 \\ S_x p \\ S_y p \\ 0 \end{pmatrix}_1, \quad (71)$$

the discrete-chemical-convective flux is defined by:

$$R_1 = |S|_1 \left\{ \frac{1}{2} M_1 \left[\begin{pmatrix} \rho_1 a \\ \rho_2 a \\ \rho_3 a \\ \rho_4 a \\ \rho_5 a \\ \rho_7 a \\ \rho_8 a \\ \rho_9 a \end{pmatrix}_L + \begin{pmatrix} \rho_1 a \\ \rho_2 a \\ \rho_3 a \\ \rho_4 a \\ \rho_5 a \\ \rho_7 a \\ \rho_8 a \\ \rho_9 a \end{pmatrix}_R \right] - \frac{1}{2} \phi_1 \left[\begin{pmatrix} \rho_1 a \\ \rho_2 a \\ \rho_3 a \\ \rho_4 a \\ \rho_5 a \\ \rho_7 a \\ \rho_8 a \\ \rho_9 a \end{pmatrix}_R - \begin{pmatrix} \rho_1 a \\ \rho_2 a \\ \rho_3 a \\ \rho_4 a \\ \rho_5 a \\ \rho_7 a \\ \rho_8 a \\ \rho_9 a \end{pmatrix}_L \right] \right\}, \tag{72}$$

and the discrete-vibrational-convective flux is determined by:

$$R_1 = |S|_1 \left\{ \frac{1}{2} M_1 \left[(\rho e_v a)_L + (\rho e_v a)_R \right] - \frac{1}{2} \phi_1 \left[(\rho e_v a)_R - (\rho e_v a)_L \right] \right\}. \tag{73}$$

The time integration is performed employing the Runge-Kutta explicit method of five stages, second-order accurate, to the three types of convective flux. To the dynamic part, this method can be represented in general form by:

$$\begin{aligned} Q_i^{(0)} &= Q_i^{(n)} \\ Q_i^{(k)} &= Q_i^{(0)} - \alpha_k \Delta t_i \, R\left(Q_i^{(k-1)}\right) / V_i \, , \\ Q_i^{(n+1)} &= Q_i^{(k)} \end{aligned} \tag{74}$$

to the chemical part, it can be represented in general form by:

$$\begin{aligned} Q_i^{(0)} &= Q_i^{(n)} \\ Q_i^{(k)} &= Q_i^{(0)} - \alpha_k \Delta t_i \left[R\left(Q_i^{(k-1)}\right) / V_i - S_C\left(Q_i^{(k-1)}\right) \right], \\ Q_i^{(n+1)} &= Q_i^{(k)} \end{aligned} \tag{75}$$

where the chemical source term S_C is calculated with the temperature T_a. Finally, to the vibrational part:

$$\begin{aligned} Q_i^{(0)} &= Q_i^{(n)} \\ Q_i^{(k)} &= Q_i^{(0)} - \alpha_k \Delta t_i \left[R\left(Q_i^{(k-1)}\right) / V_i - S_v\left(Q_i^{(k-1)}\right) \right], \\ Q_i^{(n+1)} &= Q_i^{(k)} \end{aligned} \tag{76}$$

in which:

$$S_v = \sum_{s=mol} q_{T-V,s} + \sum_{s=mol} S_{C,s} e_{v,s} \, ; \tag{77}$$

with k = 1,...,5; $\alpha_1 = 1/4$, $\alpha_2 = 1/6$, $\alpha_3 = 3/8$, $\alpha_4 = 1/2$ and $\alpha_5 = 1$. The heat flux due to translational-vibrational relaxation, $q_{T\text{-}V,s}$, is defined in Eq. (29). This scheme is first-order accurate in space and second-order accurate in time.

6 Degeneracy of CO_2, Vibrational Energy, Frozen Speed of Sound and Total Energy Equation

The CO_2 presents three levels of degeneracy, each one corresponding to a characteristic vibrational mode. The characteristic vibrational temperature and the respective degeneracy weights are given in Tab. 8.

Table 8. Values of g's and θ_v's.

Degeneracy	g	θ_v
1	1	1903.0
2	2	945.0
3	1	3329.0

Hence, the vibrational energy is determined by:

$$\begin{aligned} e_v = \sum_{s=1}^{ns} c_s e_{v,s} = \sum_{\substack{s=1 \\ s \neq 6}}^{ns} c_s e_{v,s} + g_1 c_{CO_2} e_{v,1} + g_2 c_{CO_2} e_{v,2} \\ + g_3 c_{CO_2} e_{v,3} \, , \end{aligned} \tag{78}$$

with e_v given by Eq. (27). The frozen speed of sound is given by the following equation:

$$\beta = \frac{R\sigma}{\rho c_{v,mix}} \quad \text{and} \quad a = \sqrt{\frac{(1+\beta)p}{\rho}} \, , \tag{79}$$

with:

R being the universal gas constant;

$$\sigma = \sum_{s=1}^{ns} \frac{\rho_s}{M_s} \, ; \tag{80}$$

$$c_{v,mix} = \sum_{s=1}^{ns} c_s c_{v,s} \, , \tag{81}$$

$c_{v,s}$ being the specific heat at constant volume for each species. The total energy is given by:

$$e = \rho\left[c_{v,mix} T + \left(\Delta h_{f,mix} - R_{mix} T_{ref}\right) + e_v + \frac{1}{2}\left(u^2 + v^2\right)\right], \quad (82)$$

where:

$$\Delta h_{f,mix} = \sum_{s=1}^{ns} c_s \Delta h_{f,s}\ ; \quad (83)$$

$$R_{mix} = \sum_{s=1}^{ns} c_s R_s\ ; \quad (84)$$

T_{ref} = 298.15K.

7 Initial and Boundary Conditions

7.1 Initial Condition

As initial conditions, the following flow properties are given: ρ_{init}, u_{init}, α, $T_{tr,init}$, $T_{v,init}$, $c_s(1)$, $c_s(2)$, $c_s(3)$, $c_s(4)$, $c_s(5)$, $c_s(7)$, $c_s(8)$, and $c_s(9)$, in which: α is the flow attack angle, $T_{tr,init}$ is the initial translational/rotational temperature, $T_{v,init}$ is the initial vibrational temperature, and the c_s's are the initial mass fractions of the N, O, N_2, O_2, NO, C, CO and CN. In this way, the $c_s(6)$ is easily obtained from:

$$c_s(6) = 1 - \sum_{\substack{s=1 \\ s\neq 6}}^{ns} c_s \quad (85)$$

Initially, $T_{v,init} = T_{tr,init}$. The dimensionless variables which will compose the initial vector of conserved variables are determined as follows:

$$\rho_{dim} = \rho_{init}/\rho_\infty,\ u_{dim} = u_{init}/a_{char},\ v_{dim} = u_{dim}/tg(\alpha);$$
$$T_{tr,dim} = T_{tr,init}/a_{char} \text{ and } T_{v,dim} = T_{v,init}/a_{char}, \quad (86)$$

with:

ρ_∞ defining the freestream density;

α is the flow attack angle;

a_{char} obtained from tables of the Mars atmosphere properties.

Considering the species mass fractions and with the values of the species specific heat at constant volume, it is possible to obtain the mixture specific heat at constant volume. The mixture formation enthalpy is also obtained from the mass fractions and from the species formation enthalpies. The dimensionless internal vibrational energy to each species is obtained from:

$$e_{v,dim,N_2} = R_{N_2}\theta_{v,N_2} \Big/ \left\{ e^{\left[\theta_{V,N_2}/T_{V,dim}\right]} - 1 \right\};$$
$$e_{v,dim,O_2} = R_{O_2}\theta_{v,O_2} \Big/ \left\{ e^{\left[\theta_{V,O_2}/T_{V,dim}\right]} - 1 \right\};$$
$$e_{v,dim,NO} = R_{NO}\theta_{v,NO} \Big/ \left\{ e^{\left[\theta_{V,NO}/T_{V,dim}\right]} - 1 \right\};$$
$$e_{v,dim,CO_2(1)} = g(1)\times R_{CO_2}\theta_{v,CO_2(1)} \Big/ \left\{ e^{\left[\theta_{V,CO_2(1)}/T_{V,dim}\right]} - 1 \right\};$$
$$e_{v,dim,CO_2(2)} = g(2)\times R_{CO_2}\theta_{v,CO_2(2)} \Big/ \left\{ e^{\left[\theta_{V,CO_2(2)}/T_{V,dim}\right]} - 1 \right\};$$
$$e_{v,dim,CO_2(3)} = g(3)\times R_{CO_2}\theta_{v,CO_2(3)} \Big/ \left\{ e^{\left[\theta_{V,CO_2(3)}/T_{V,dim}\right]} - 1 \right\};$$
$$e_{v,dim,CO} = R_{CO}\theta_{v,CO} \Big/ \left\{ e^{\left[\theta_{V,CO}/T_{V,dim}\right]} - 1 \right\};$$
$$e_{v,dim,CN} = R_{CN}\theta_{v,CN} \Big/ \left\{ e^{\left[\theta_{V,CN}/T_{V,dim}\right]} - 1 \right\}. \quad (87)$$

The total internal vibrational energy of the system is determined by Eq. (28). Finally, the dimensionless total energy is determined by Eq. (82). The initial vector of conserved variables is, therefore, defined by:

$$Q = \begin{Bmatrix} \rho_{dim} \\ \rho_{dim} u_{dim} \\ \rho_{dim} v_{dim} \\ e_{dim} \\ \rho_{dim} c_s(1) \\ \rho_{dim} c_s(2) \\ \rho_{dim} c_s(3) \\ \rho_{dim} c_s(4) \\ \rho_{dim} c_s(5) \\ \rho_{dim} c_s(7) \\ \rho_{dim} c_s(8) \\ \rho_{dim} c_s(9) \\ \rho_{dim} e_{v,dim} \end{Bmatrix}. \quad (88)$$

7.2 Boundary Conditions

(a) Dynamical Part:

The boundary conditions are basically of three types: solid wall, entrance and exit. These conditions are implemented in special cells, named ghost cell.

(a.1) Wall condition: This condition imposes the flow tangency at the solid wall. This condition is satisfied considering the wall tangent velocity component of the ghost volume as equals to the respective velocity component of its real neighbor cell. At the same way, the wall normal velocity component of the ghost cell is equaled in value, but with opposite signal, to the respective velocity component of the real neighbor cell. It results in:

$$n_x = \Delta y/\sqrt{\Delta x^2 + \Delta y^2}; \quad (89)$$
$$n_y = -\Delta x/\sqrt{\Delta x^2 + \Delta y^2}; \quad (90)$$

where, for the (i+1/2,j) interface:

$$\Delta x = x_{i+1,j+1} - x_{i+1,j}; \quad (91)$$
$$\Delta y = y_{i+1,j+1} - y_{i+1,j}. \quad (92)$$

Hence, the ghost cell velocity components are written as:

$$u_g = \left(n_y^2 - n_x^2\right)u_r - (2n_x n_y)v_r; \quad (93)$$
$$v_g = -(2n_x n_y)u_r + \left(n_y^2 - n_x^2\right)v_r, \quad (94)$$

with "g" related with ghost cell and "r" related with real cell. To the viscous case, the boundary condition imposes that the ghost cell velocity components be equal to the real cell velocity components, with the negative signal:

$$u_g = -u_r; \quad (95)$$
$$v_g = -v_r, \quad (96)$$

The pressure gradient normal to the wall is assumed be equal to zero, following an inviscid formulation and according to the boundary layer theory. The same hypothesis is applied to the temperature gradient normal to the wall, considering adiabatic wall. The ghost volume density and pressure are extrapolated from the respective values of the real neighbor volume (zero order extrapolation), with these two conditions. The total energy is obtained by the state equation of a perfect gas.

(a.2) Entrance condition:
(a.2.1) Subsonic flow: Three properties are specified and one is extrapolated, based on analysis of information propagation along characteristic directions in the calculation domain ([28]). In other words, three characteristic directions of information propagation point inward the computational domain and should be specified. Only the characteristic direction associated to the "(q_n-a)" velocity cannot be specified and should be determined by interior information of the calculation domain. The total energy was the extrapolated variable from the real neighbor volume, to the studied problems. Density and velocity components had their values determined by the initial flow properties.
(a.2.2) Supersonic flow: All variables are fixed with their initial flow values.

(a.3) Exit condition:
(a.3.1) Subsonic flow: Three characteristic directions of information propagation point outward the computational domain and should be extrapolated from interior information ([28]). The characteristic direction associated to the "(q_n-a)" velocity should be specified because it penetrates the calculation domain. In this case, the ghost volume's total energy is specified by its initial value. Density and velocity components are extrapolated.
(a.3.2) Supersonic flow: All variables are extrapolated from the interior domain due to the fact that all four characteristic directions of information propagation of the Euler equations point outward the calculation domain and, with it, nothing can be fixed.

(b) Chemical Part:
The boundary conditions to the chemical part are also of three types: solid wall, entrance and exit.

(b.1) Wall condition: In both inviscid and viscous cases, the non-catalytic wall condition is imposed, which corresponds to a zero order extrapolation of the species density from the neighbor real cells.

(b.2) Entrance condition: In this case, the species densities of each ghost cell are fixed with their initial values (freestream values).

(b.3) Exit condition: In this case, the species densities are extrapolated from the values of the neighbor real cells.

(c) Vibrational Part:
The boundary conditions in the vibrational part are also of three types: solid wall, entrance and exit.

(c.1) Wall condition: In both inviscid and viscous cases, the internal vibrational energy of the ghost cell is extrapolated from the value of its neighbor real cell.

(c.2) Entrance condition: In this case, the internal vibrational energy of each ghost cell is fixed with its initial value (freestream value).

(c.3) Exit condition: In this case, the internal vibrational energy is extrapolated from the value of the neighbor real cell.

8 Spatially Variable Time Step

The basic idea of this procedure consists in keeping constant the CFL number in all calculation domain, allowing, hence, the use of appropriated time steps to each specific mesh region during the convergence process. According to the definition of the CFL number, it is possible to write:

$$\Delta t_{i,j} = CFL(\Delta s)_{i,j} / c_{i,j} , \qquad (97)$$

where CFL is the "Courant-Friedrichs-Lewy" number to provide numerical stability to the scheme; $c_{i,j} = \left[\left(u^2 + v^2 \right)^{0.5} + a \right]_{i,j}$ is the maximum characteristic speed of information propagation in the calculation domain; and $(\Delta s)_{i,j}$ is a characteristic length of information transport. On a finite volume context, $(\Delta s)_{i,j}$ is chosen as the minor value found between the minor centroid distance, involving the (i,j) cell and a neighbor, and the minor cell side length.

9 Configurations and Employed Meshes

Figures 3 and 4 present the employed meshes to the structured simulations in two-dimensions for the reactive flow around the blunt body. Figure 3 shows the structured mesh to inviscid simulations, whereas Fig. 4 presents the structured mesh to viscous simulations. The viscous case mesh exhibits an exponential stretching in the η direction with a value of 7.5%. The inviscid case mesh has 3,776 rectangular cells and 3,900 nodes, which corresponds in finite differences to a mesh of 65x60 points. The viscous case mesh has the same number of rectangular cells and nodes.

Figures 5 and 6 present the employed meshes applied to the unstructured simulations in two-dimensions for the reactive flow around the studied blunt body. Figure 5 shows the unstructured mesh to the inviscid simulations, whereas Fig. 6 exhibits the unstructured mesh to the viscous simulations. The viscous case mesh presents an exponential stretching of 7,5% in the η direction. In the inviscid case, a mesh of 7,552 triangular cells and 3,900 nodes is employed, which corresponds to a mesh of 65x60 points in finite differences.

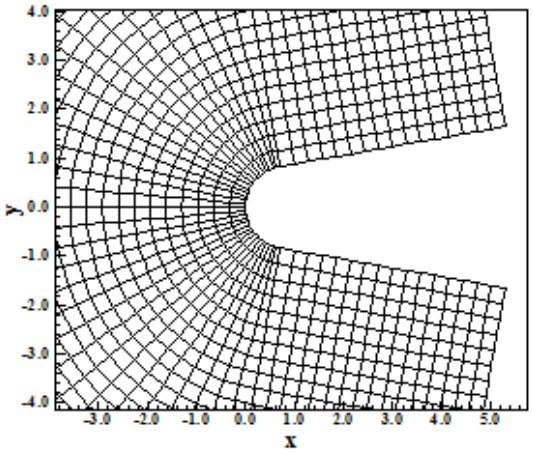

Figure 3. 2D structured mesh for inviscid flow.

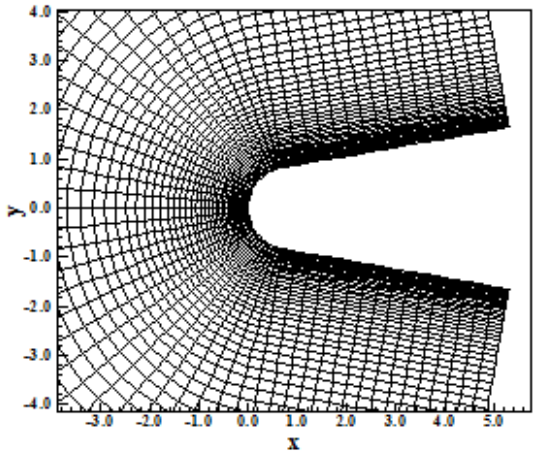

Figure 4. 2D structured mesh for viscous flow.

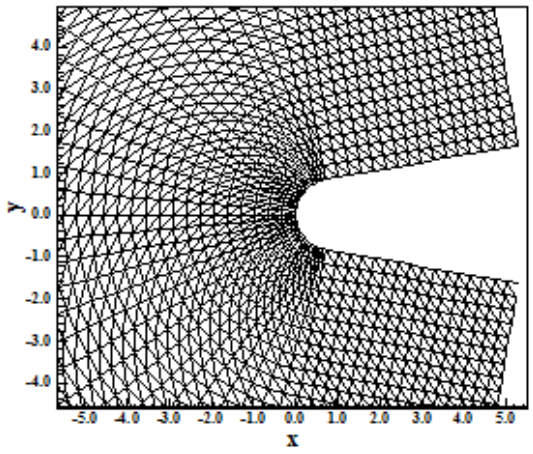

Figure 5. 2D unstructured mesh for inviscid flow.

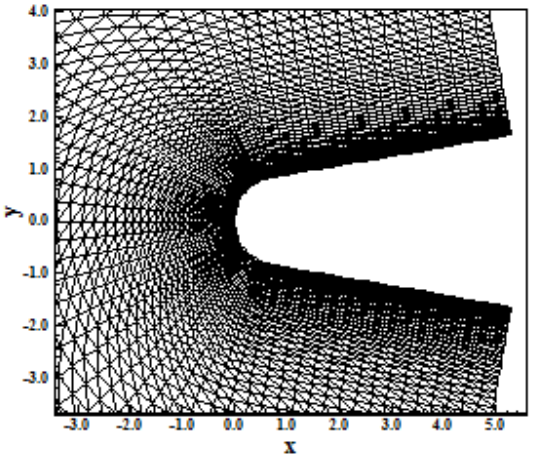

Figure 6. 2D unstructured mesh for viscous flow.

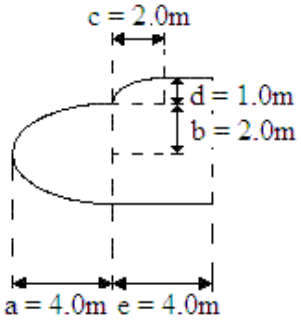

Figure 7. Double ellipse configuration.

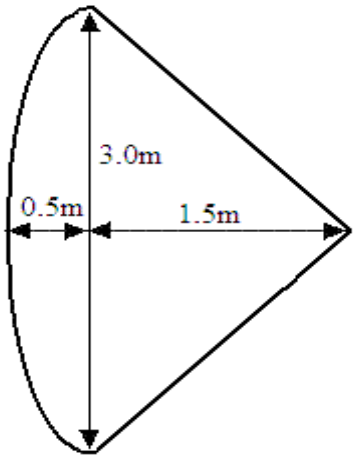

Figure 8. Entry capsule configuration.

In the viscous case, the same number of triangular cells and grid points is showed, corresponding to a finite difference mesh of 65x60 points. The unstructured meshes are obtained transforming a mesh of quadrilaterals in a mesh of triangles and the connectivity, neighboring, ghost and node coordinate tables are generated in a pre-processing stage of the computation.

Figures 7 and 8 exhibit the geometrical configurations of the double ellipse and of the entry capsule. In Figure 7 is presented the double ellipse configuration and in Fig. 8 is presented the entry capsule configuration.

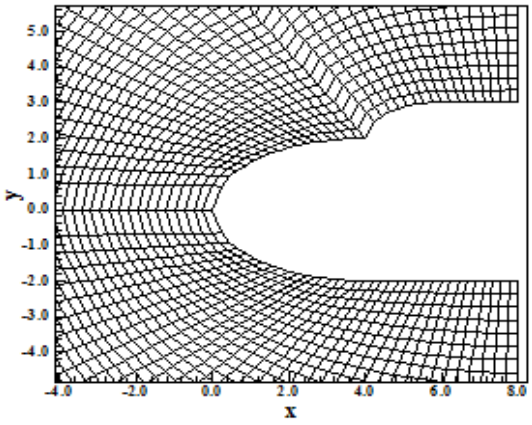

Figure 9. 2D structured mesh for inviscid case.

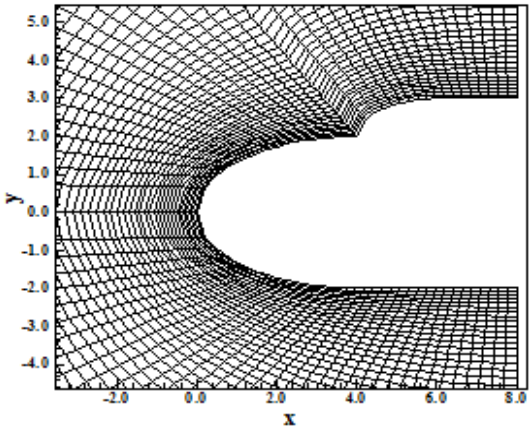

Figure 10. 2D structured mesh for viscous flow.

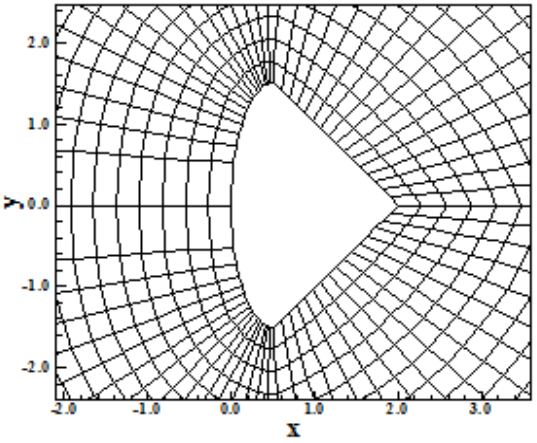

Figure 11. 2D structured mesh for inviscid flow.

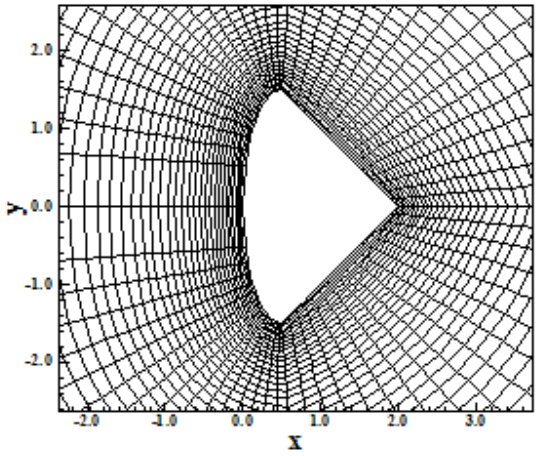

Figure 12. 2D structured case for viscous flow.

The double ellipse mesh is composed of 3,528 rectangular cells and 3,650 nodes in the structured case and of 7,056 triangular cells and 3,650 nodes in the unstructured case. The entry capsule is composed of 3,136 rectangular cells and 3,250 nodes in the structured case. The unstructured case is not studied for this problem.

Figures 9 and 10 present the inviscid and viscous double ellipse structured meshes, whereas Figs. 11 and 12 present the inviscid and viscous entry capsule structured meshes. As aforementioned, two unstructured cells are obtained dividing each rectangular cell into two triangular cells, with the generation of the respective tables.

10 Results

Tests were performed in a notebook with INTEL PENTIUM Dual Core processors of 2.30GHz and 2GBytes of RAM. As the interest of this work is steady state problems, it is necessary to define a criterion which guarantees the convergence of the numerical results. The criterion adopted was to consider a reduction of no minimal three (3) orders of magnitude in the value of the maximum residual in the calculation domain, a typical CFD-community criterion. In the simulations, the attack angle was set equal to zero.

10.1 Blunt Body Problem

The initial conditions are presented in Tab. 9. The Reynolds number is obtained from data available in the Mars atmosphere tables [30]. The geometry of this problem is a blunt body with 0.85m of nose ratio and rectilinear walls with 10º inclination. The far field is located at 20.0 times the nose ratio in relation to the configuration nose.

Table 9. Initial conditions to the blunt body problem.

Property	Value
M_∞	31.0
ρ_∞	0.0002687 kg/m^3
p_∞	8.3039 Pa
U_∞	6,155 m/s
T_∞	160.9 K
Altitude	41,700 m
c_N	0.00
c_O	0.00
c_{N_2}	0.03
c_{O_2}	0.00
c_{NO}	0.00
c_{CO_2}	0.97
c_C	0.00
c_{CO}	0.00
c_{CN}	0.00
L	1.7 m
Re_∞	3.23x10^5

10.1.1 Inviscid, first order, structured results

Figures 13 and 14 exhibit the pressure contours obtained by [2] and [22], respectively. As can be observed, the [2] pressure field is more severe than the [22] pressure field. Good symmetry characteristics are observed in both figures.

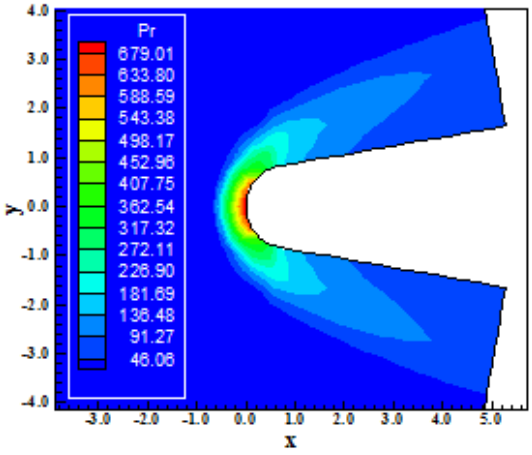

Figure 13. Pressure contours ([2]).

Figures 15 and 16 present the Mach number contours captured by [2] and [22], respectively. Good symmetry properties are observed in both figures. Quantitatively, there are no meaningful differences between the two fields. Both peaks are very high and an appropriate thermal protection is necessary to guarantee the integrity of the spatial vehicle. This thermal protection should be located

mainly in the blunt nose, which receives the main contribution of the heating. To this range of temperature, the main heating contribution is due to radiation and a blunt slender profile is recommended to reduce such effect, as was used in this example.

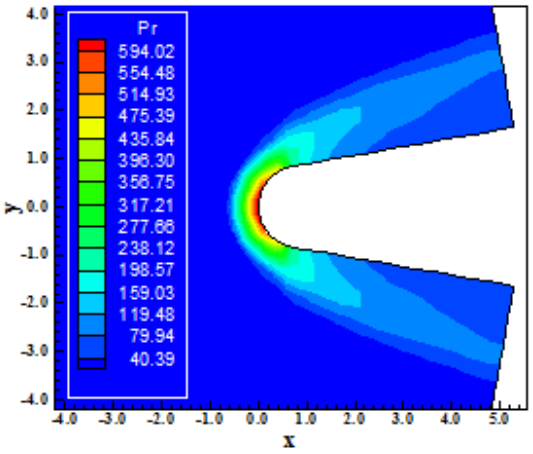

Figure 14. Pressure contours ([22]).

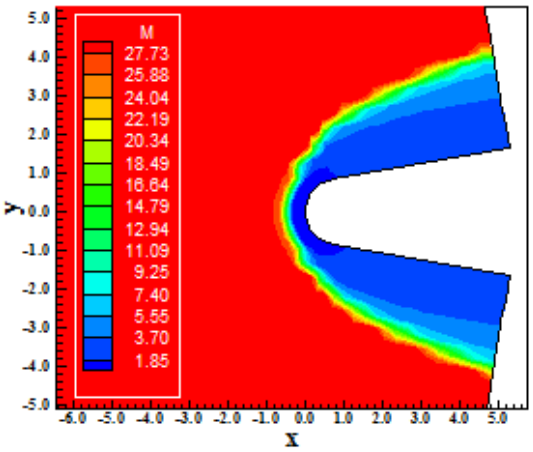

Figure 15. Mach number contours ([2]).

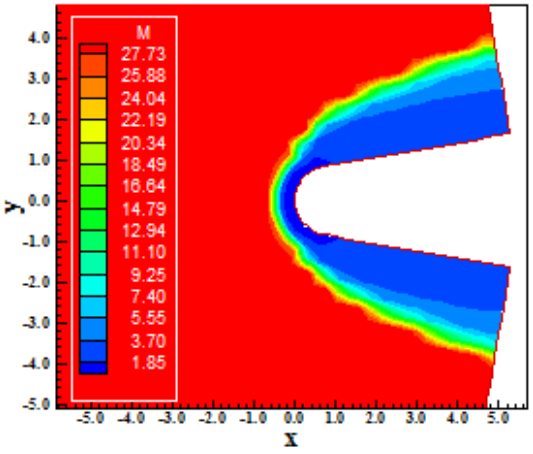

Figure 16. Mach number contours ([22]).

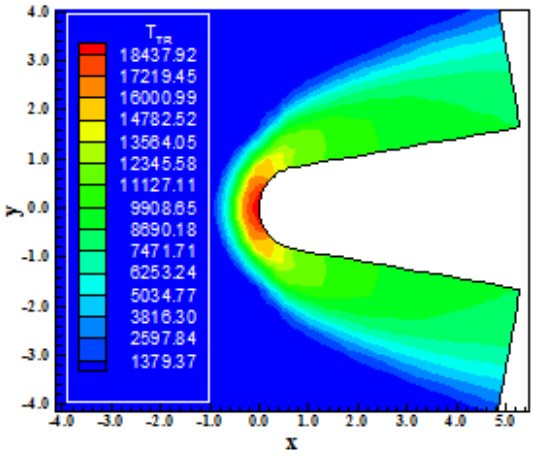

Figure 17. Translational/Rotational temperature contours ([2]).

Figures 17 and 18 show the translational/rotational temperature contours obtained by [2] and [22], respectively. As can be observed, the temperatures are very high in comparison with the temperatures observed in reentry flows in earth ([27]). The [2] scheme captures a temperature peak of 18,438K, whereas the [22] scheme captures a temperature peak of 16,370K.

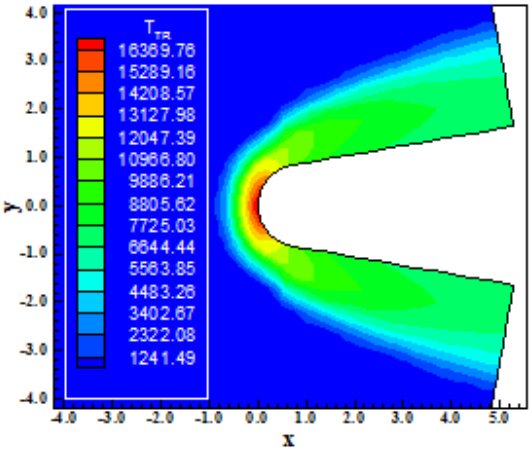

Figure 18. Translational/Rotational temperature contours ([22]).

Figures 19 and 20 exhibit the vibrational temperature contours captured by [2] and [22], respectively. As can be seen, the most severe vibrational temperature is presented by the [22] solution. The solution presented by the [2] scheme is less intense than the [22] solution. Moreover, the [2] solution is smoother, whereas the [22] solution presents wiggles close to the inclined walls/blunt nose interface regions.

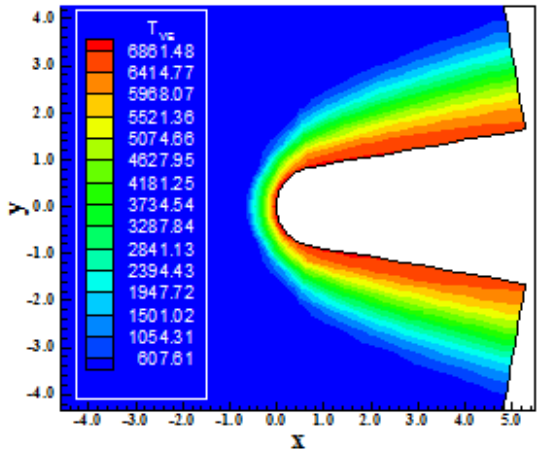

Figure 19. Vibrational temperature contours ([2]).

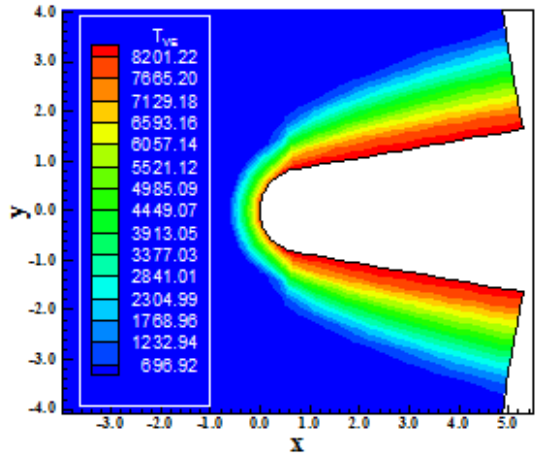

Figure 20. Vibrational temperature contours ([22]).

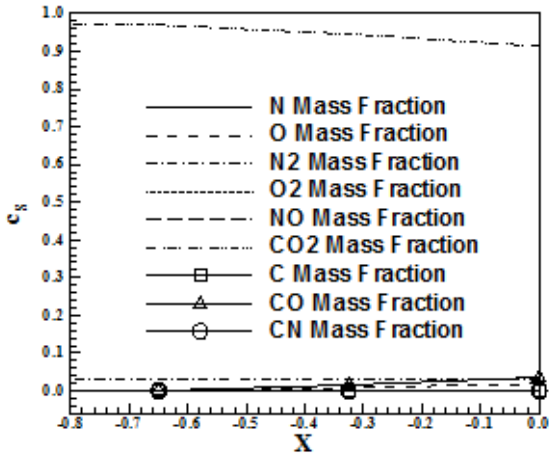

Figure 21. Mass fraction distributions at the stagnation line ([2]).

Figure 21 shows the mass fraction distributions at the stagnation line of the blunt body, generated by [2]. As can be seen, a significant dissociation of CO_2 occurs, with meaningful formation of CO. It is also observed an important increase of N_2 and formation of O.

Figure 22 presents the mass fraction distributions of the nine species along the body stagnation line, generated by [22]. As in [2] solution, a significant CO_2 dissociation occurs close to the body and, more distinguishable, is the formation of CO, in relation to the [2] solution. It is also possible to note the significant formation of the O, due mainly to the CO_2 dissociation.

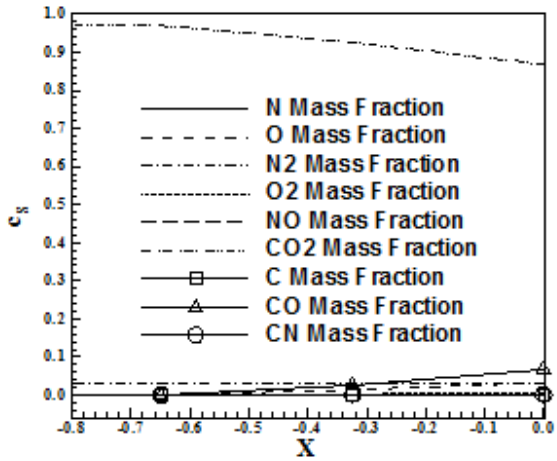

Figure 22. Mass fraction distributions at the stagnation line ([22]).

10.1.2 Viscous, first order, structured results

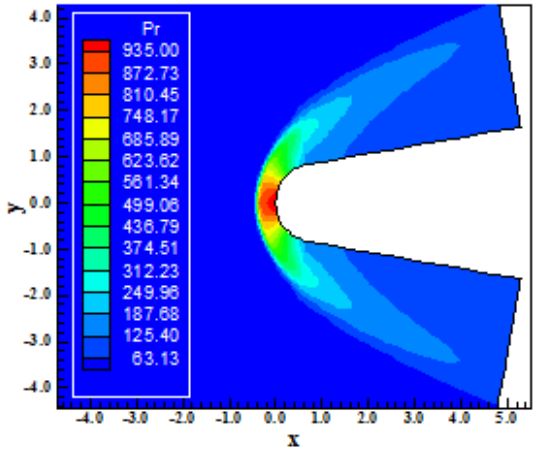

Figure 23. Pressure contours ([2]).

Figures 23 and 24 exhibit the pressure contours obtained by [2] and [22], respectively, in the viscous case. As can be observed, the pressure field generated by the [2] solution is more severe than that generated by the [22] solution. Moreover, the shock region generated by the [22] scheme is closest to the blunt nose than the same region generated by the [2] scheme. This behavior suggests that the

shock profile of the [22] scheme is more realistic, closest to the blunt nose. The shock is generated more precisely by both schemes and with better characteristics than the inviscid shock.

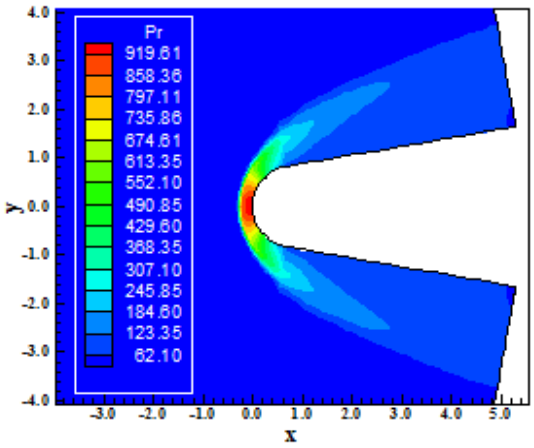

Figure 24. Pressure contours ([22]).

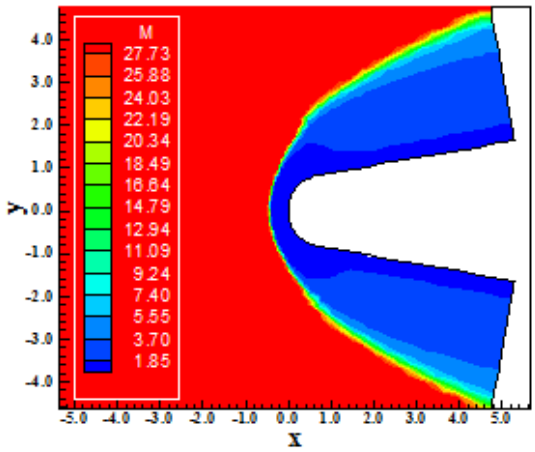

Figure 25. Mach number contours ([2]).

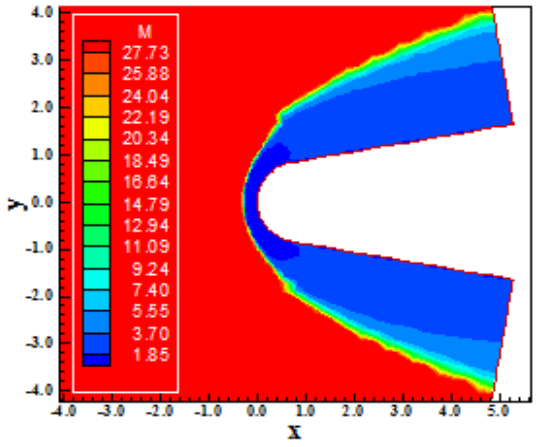

Figure 26. Mach number contours ([22]).

Figures 25 and 26 present the Mach number contours obtained by [2] and [22], respectively. The [2] solution is more dissipative, generating bigger regions of supersonic flow, close to the wall. Quantitatively, there are not meaningful differences.

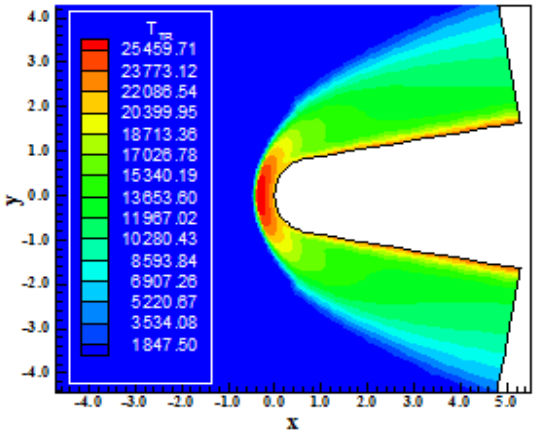

Figure 27. Translational/Rotational temperature contours ([2]).

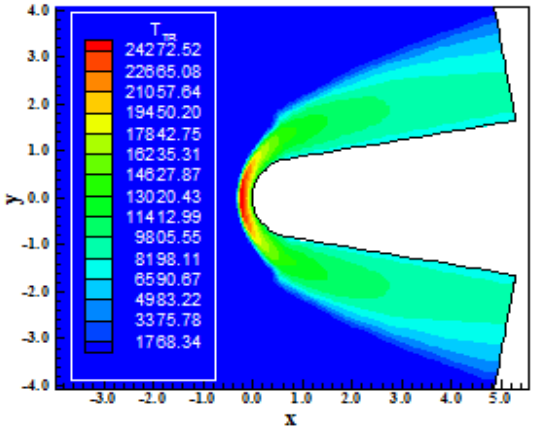

Figure 28. Translational/Rotational temperature contours ([22]).

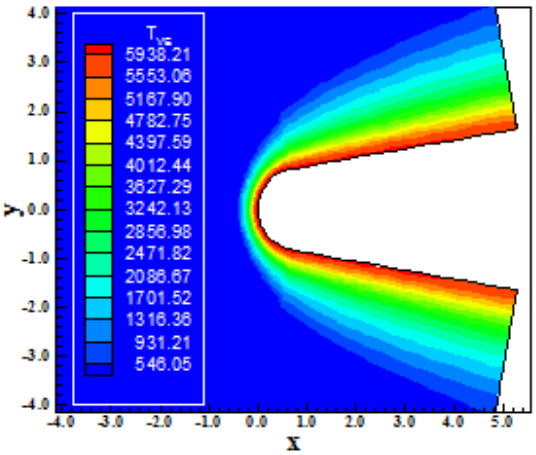

Figure 29. Vibrational temperature contours ([2]).

Figures 27 and 28 exhibit the translational/rotational temperature contours

generated by the [2] and [22], respectively. In this viscous case, temperatures peaks above 24,000K are observed. In this range, the radiation heat transfer phenomenon is predominant and justifies the use of a blunt slender body to fly at the Mars atmosphere. The normal shock wave generated by the [2] scheme is more symmetrical and heater than the [22] one.

Figures 29 and 30 show the vibrational temperature contours obtained by [2] and [22], respectively. The vibrational temperature contours generated by the [22] scheme are higher than the respective ones due to [2]. Moreover, the shock layer is confined to a smaller region, close to the wall, than the [2] shock layer region.

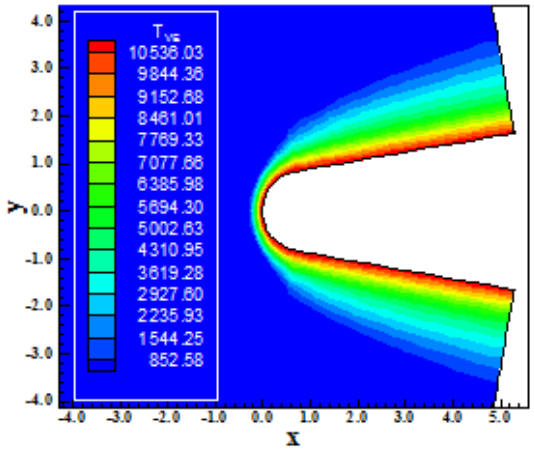

Figure 30. Vibrational temperature contours ([22]).

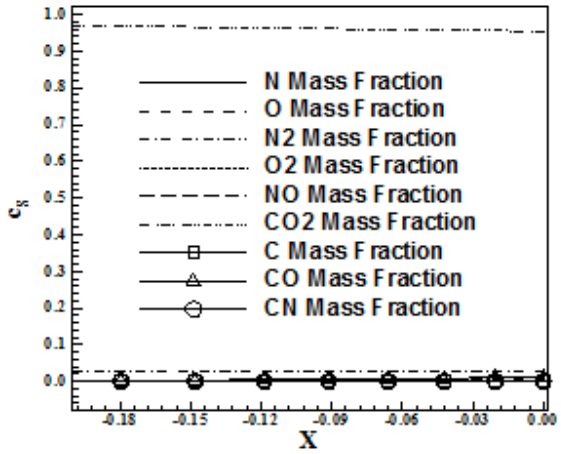

Figure 31. Mass fraction distributions at the stagnation line ([2]).

Figure 31 exhibits the mass fraction distributions of the nine species obtained from the [2] scheme. A discrete dissociation of the CO_2 is observed. As also noted the formations of CO and O are also seen, being more discrete than the dissociation of CO_2.

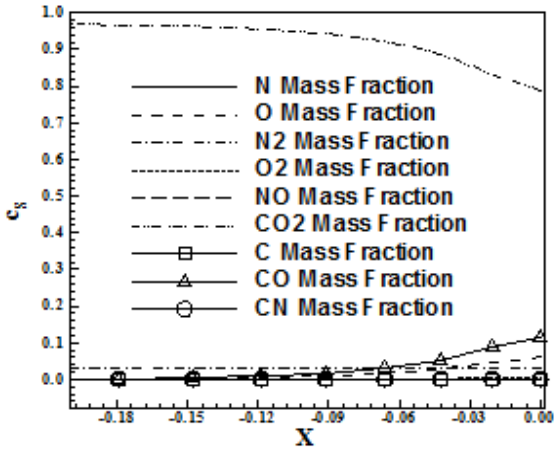

Figure 32. Mass fraction distributions at the stagnation line ([22]).

Figure 32 shows the mass fraction distributions of the nine species obtained from the [22] scheme. A significant dissociation of CO_2 is seen. The production of CO is also very meaningful, as also the formation of O, mainly due to the dissociation of CO_2. It is also noted the increase in the N_2 formation.

10.1.3 Inviscid, second order, structured results

Figures 33 and 34 show the pressure contours obtained by [2] and [22], respectively. The most strength pressure field is due to [2]. Both solutions present good symmetry properties. The pressure peak due to [2] reaches a value of 664 unities, whereas this peak due to [22] reaches a value of 553.

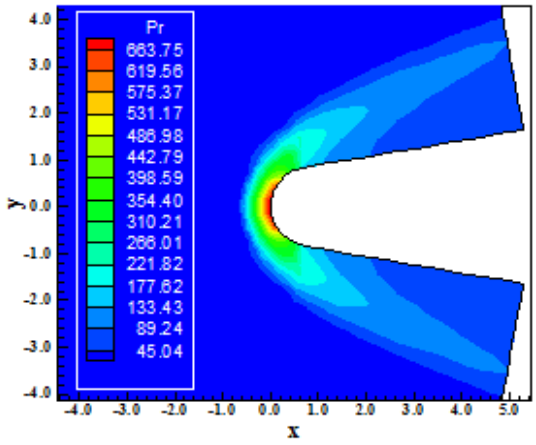

Figure 33. Pressure contours ([2]).

Figures 35 and 36 present the Mach number contours due to [2] and [22], respectively. The two Mach number fields are very similar, quantitatively

and qualitatively. The region of supersonic field is more extent in the [2] solution.

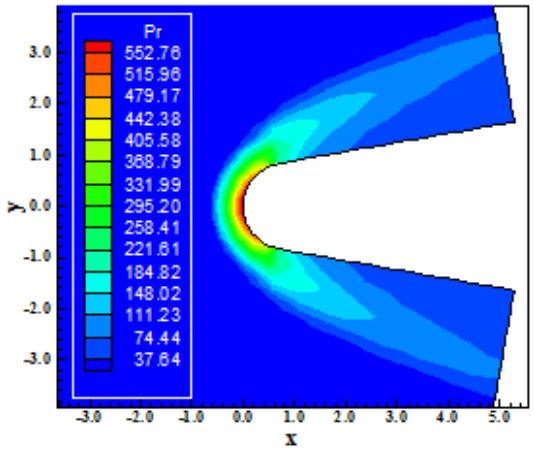

Figure 34. Pressure contours ([22]).

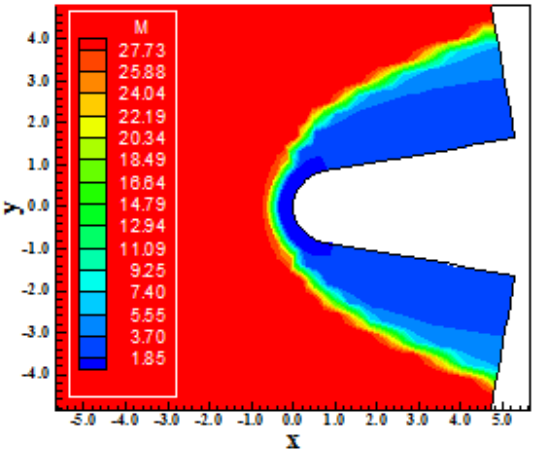

Figure 35. Mach number contours ([2]).

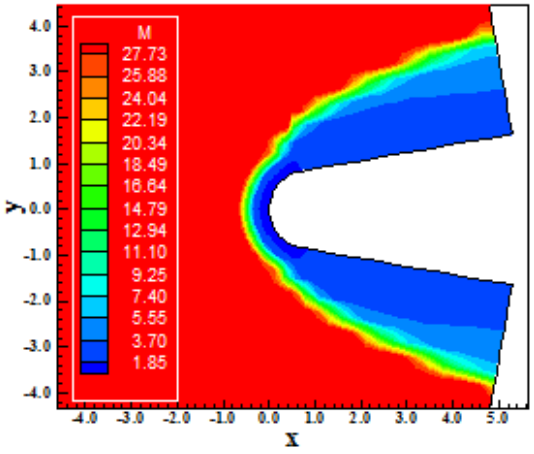

Figure 36. Mach number contours ([22]).

Figures 37 and 38 show the translational/rotational temperature contours obtained by [2] and [22], respectively. The temperature fields due to [2] and [22] reach maximum peaks of 20,840K and 17,233K, less intense than in the inviscid results. Again these peaks are concentrated in the blunt nose region.

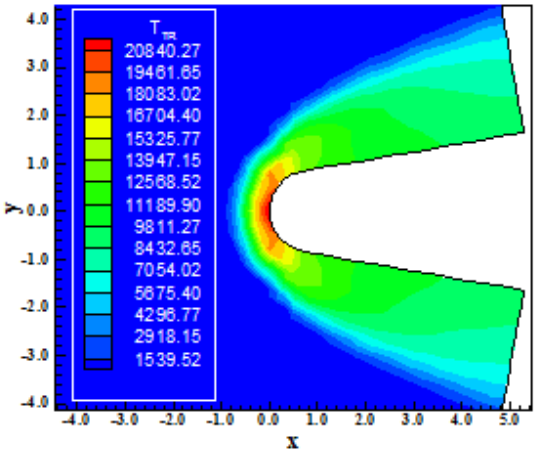

Figure 37. Translational/Rotational temperature contours ([2]).

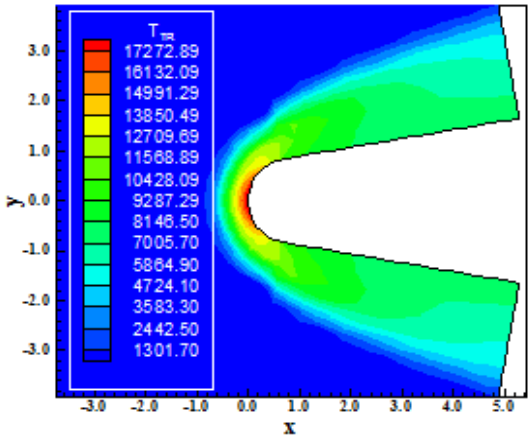

Figure 38. Translational/Rotational temperature contours ([22]).

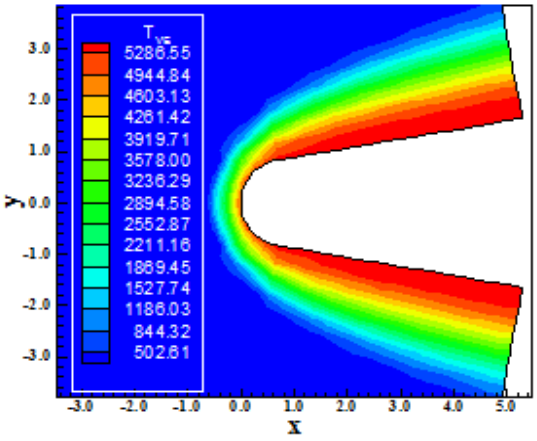

Figure 39. Vibrational temperature contours ([2]).

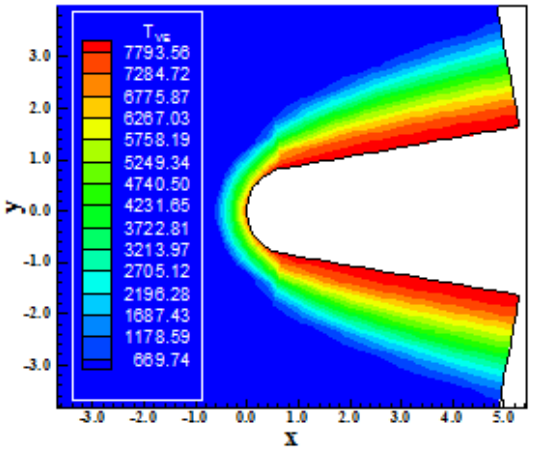

Figure 40. Vibrational temperature contours ([22]).

Figures 39 and 40 show the vibrational temperature contours obtained [2] and [22], respectively. The hot shock layer of the [22] solution is confined to a smaller region than the hot shock layer of the [2] solution. The [2] solution is smoother than the [22] one. Moreover, the [22] solution is more intense than the respective one of [2].

The 41 exhibits the mass fraction distributions along the body stagnation line obtained by the [2] scheme. Again a very discrete dissociation of the CO_2 is observed. The formation of CO and O are also very discrete.

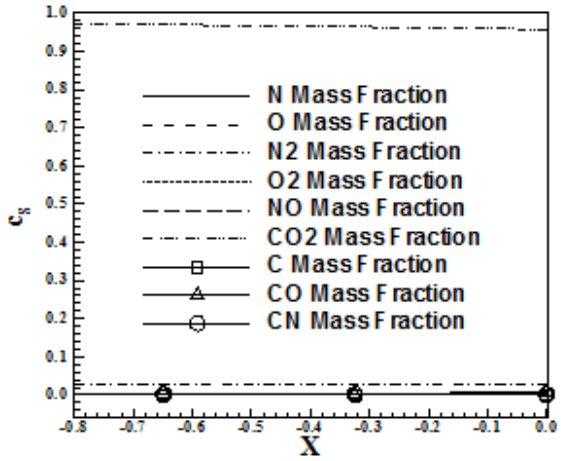

Figure 41. Mass fraction distributions at the stagnation line ([2]).

Figure 42 presents the mass fraction distributions generated by the [22] algorithm. It is possible to note a more significant CO_2 dissociation than in the [2] case. As a consequence, the CO and O formations are also more pronounced in relation to the [2] solution. The production of C and CN are less pronounced.

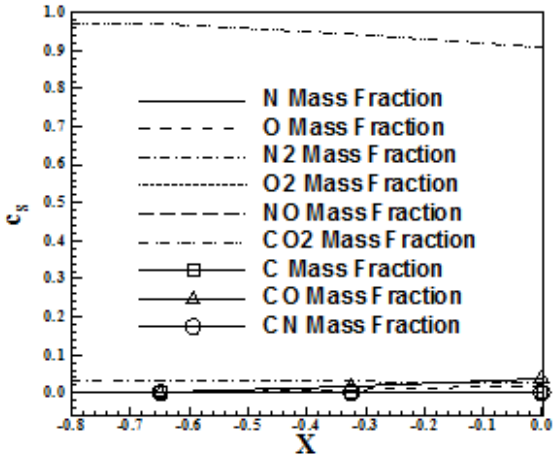

Figure 42. Mass fraction distributions at the stagnation line ([22]).

10.1.4 Viscous, second order, structured results

Figures 43 and 44 exhibit the pressure contours obtained by [2] and [22], respectively. The shock wave, in both cases, is well captured. The solution of [22] estimates a minor shock standoff distance. Good symmetry properties are observed in both solutions. The [2] pressure field is again more severe than that generated by [22].

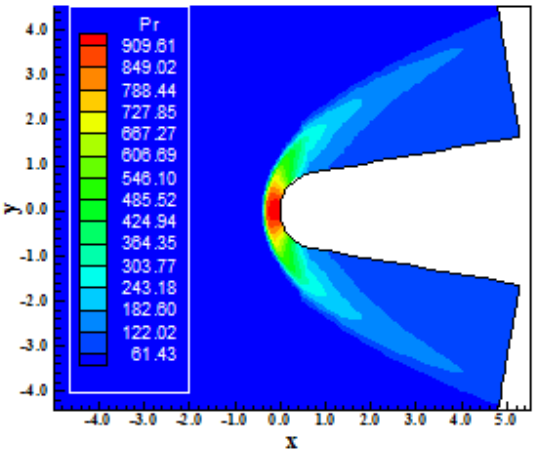

Figure 43. Pressure contours ([2]).

Figures 45 and 46 show the Mach number contours generated by [2] and [22], respectively. As can be observed, the [2] scheme is more dissipative, spreading the low supersonic region around the body, whereas the [22] scheme only allows the low supersonic region at the body nose.

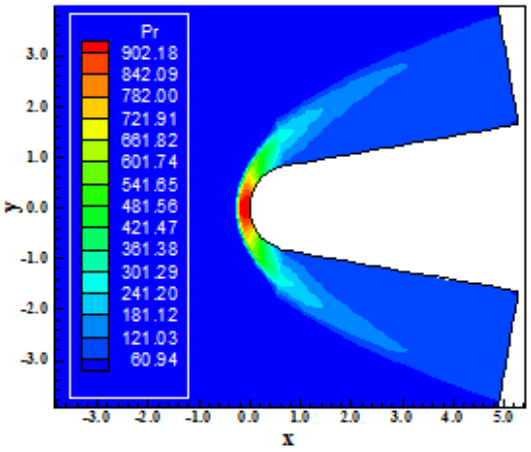

Figure 44. Pressure contours ([22]).

The contours of Mach number due to [2] are more symmetrical than those of [22]. The shock wave develops correctly, passing from a normal shock wave, going to oblique shock waves and finishing with Mach waves.

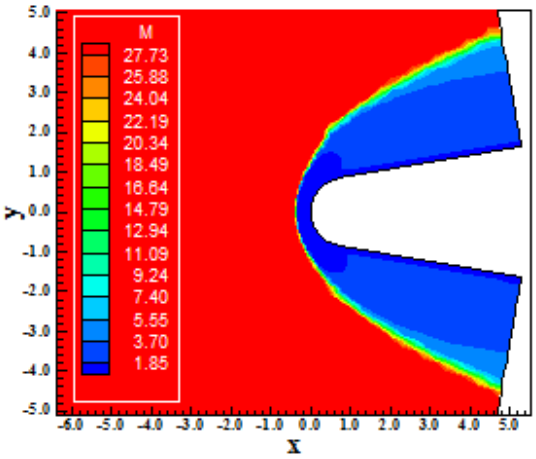

Figure 45. Mach number field ([2]).

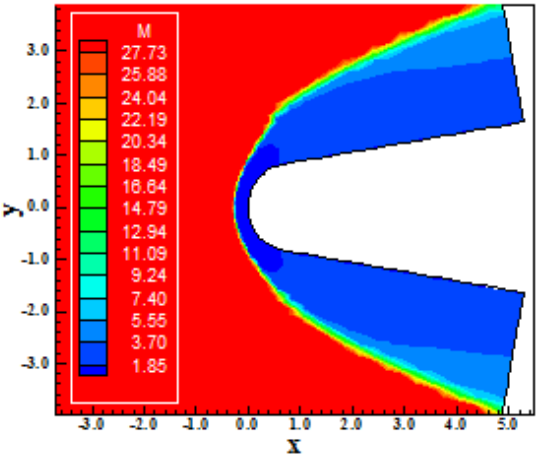

Figure 46. Mach number field ([22]).

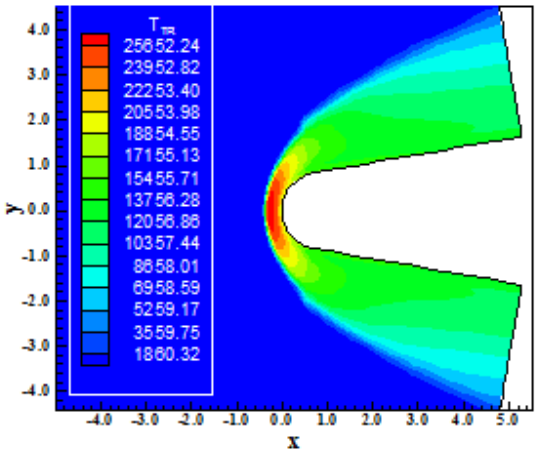

Figure 47. Translational/Rotational temperature contours ([2]).

Figures 47 and 48 show the translational/rotational temperature contours obtained by [2] and [22], respectively. Both temperature fields are close to 25,000K. It is clear the high temperature at the body nose, mainly in the [2] scheme.

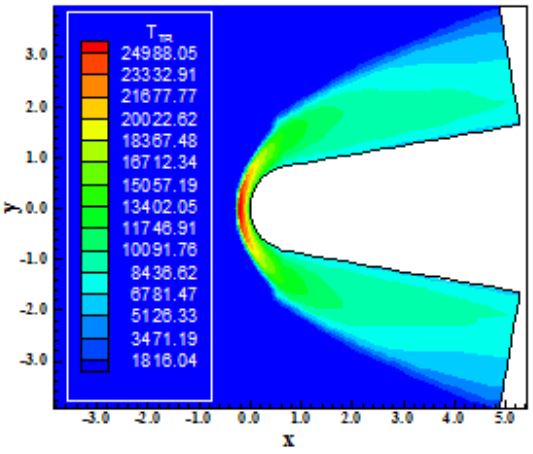

Figure 48. Translational/Rotational temperature contours ([22]).

Figures 49 and 50 present the vibrational temperature contours obtained from [2] and [22], respectively. The [22] solution presents the highest temperature peak at the nose and along the body. The [2] solution presents a less severe temperature field. The shock layer of [22] is confined to a minor region than the respective one of the [2] scheme.

Figure 51 exhibits the mass fraction distributions along the stagnation line of the blunt body, generated by [2] scheme. As can be seen, a discrete dissociation of CO_2 is captured by the [2] scheme, with minor formation of CO and O. Figure 52 shows

the mass fraction distributions along the stagnation line of the blunt body, captured by the [22] scheme. In this solution, a significant CO2 dissociation is observed, with meaningful formation of CO and O.

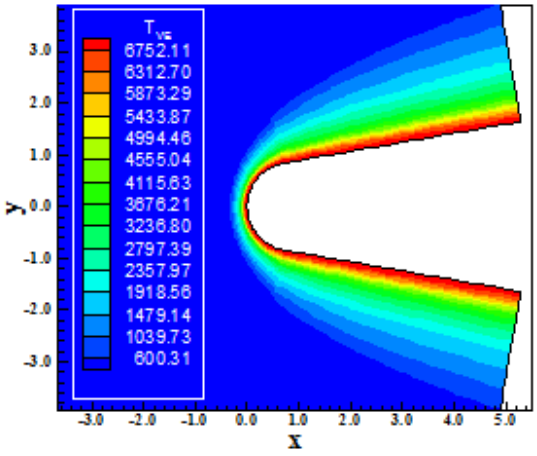

Figure 49. Vibrational temperature contours ([2]).

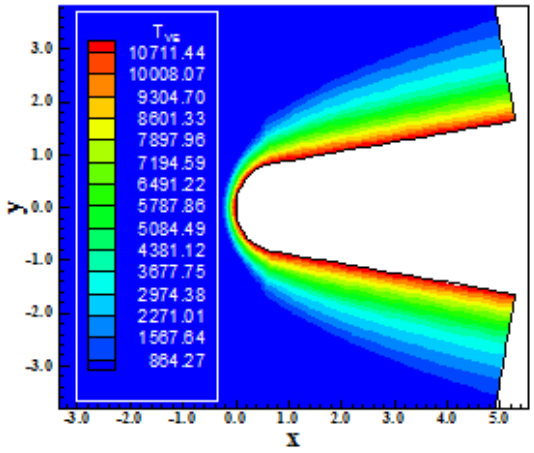

Figure 50. Vibrational temperature contours ([22]).

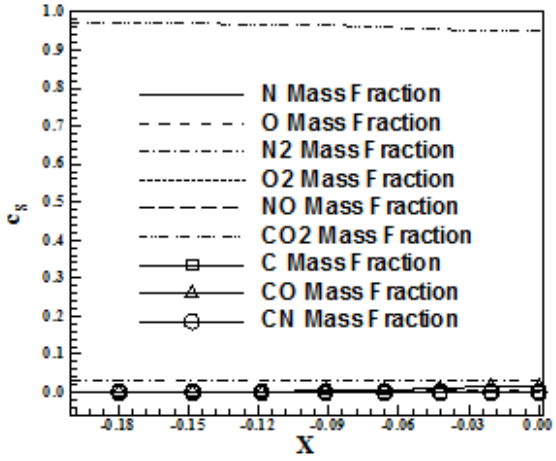

Figure 51. Mass fraction distributions at the stagnation line ([2]).

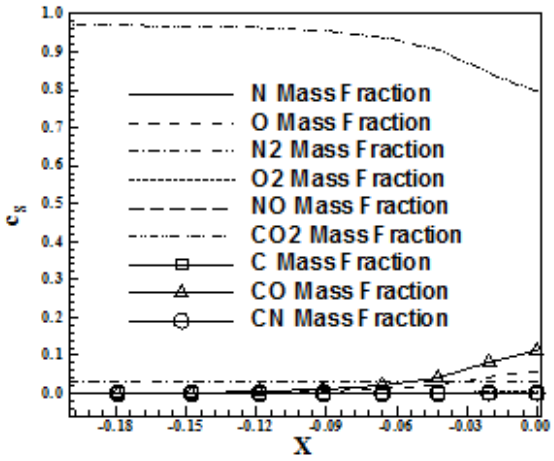

Figure 52. Mass fraction distributions at the stagnation line ([22]).

10.1.5 Inviscid, first order, unstructured results

In the unstructured case, only the [22] scheme yielded converged results. Figure 53 shows the pressure contours obtained by [22] algorithm. The non-symmetry is typical of unstructured solutions. The pressure peak is greater than the first order, inviscid, structured, [22] counterpart solution.

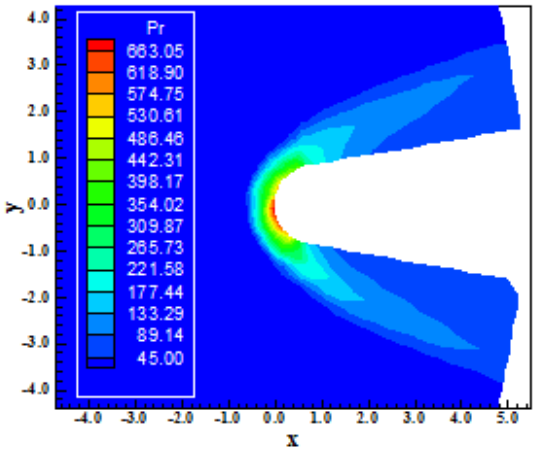

Figure 53. Pressure contours ([22]).

Figure 54 exhibits the Mach number contours obtained by the [22] unstructured scheme. The subsonic region behind the shock is well characterized. Non-symmetry is also detected in this solution, but the shock wave pass from normal shock, through oblique shock waves until Mach wave far from the body. There are non-oscillations or pre-shock oscillations in the solution.

Figure 55 presents the translational/rotational temperature contours obtained by [22]. The temperature peak reaches a value of 18,367 K, comparable to the respective values obtained in the

structured case. Non-symmetry aspects are also observed in this solution, mainly at the nose region.

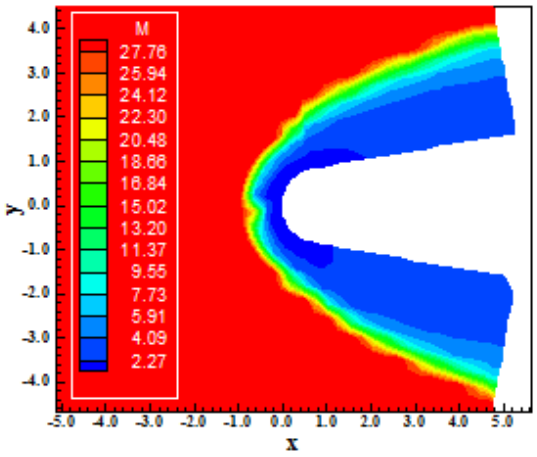

Figure 54. Mach number contours ([22]).

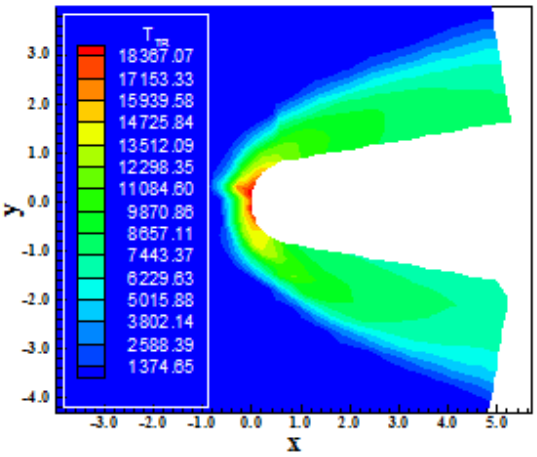

Figure 55. Translational/Rotational temperature contours ([22]).

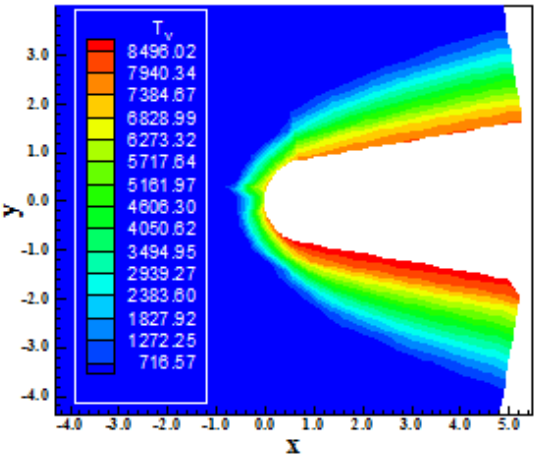

Figure 56. Vibrational temperature contours ([22]).

Figure 56 exhibits the vibrational temperature contours. There is a heating at the body surface, mainly at the lower wall surface, captured by the scheme. The vibrational temperature peak is 8,496 K, far lower than the translational/rotational temperature.

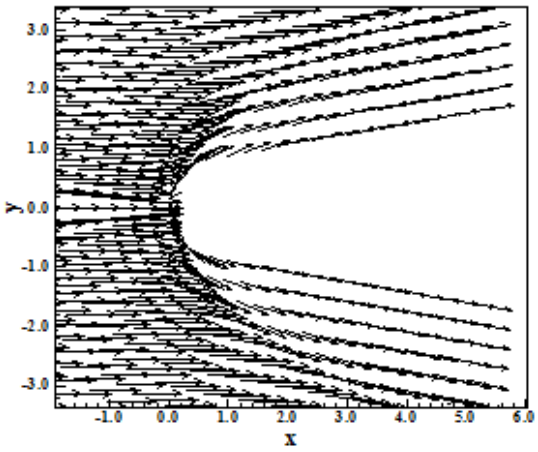

Figure 57. Velocity vector field.

Figure 57 presents the velocity vector field obtained by the [22] scheme around the blunt body geometry. The tangency condition is well satisfied by the solution of the numerical scheme.

10.1.6 Viscous, first order, unstructured results

Figure 58 exhibits the pressure contours obtained by the [22] scheme. The pressure peak reaches a value of 919 unities. Good symmetry characteristics are observed. The shock is well close to the blunt nose.

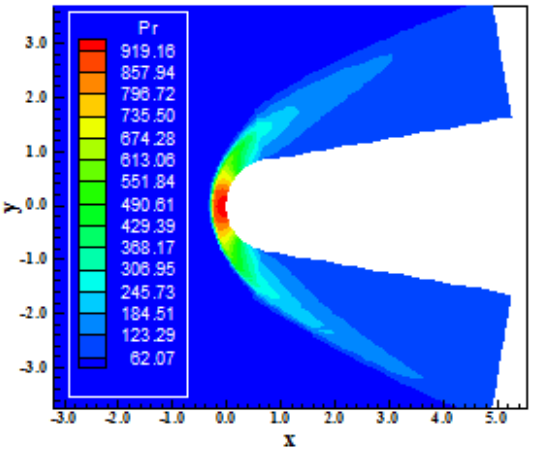

Figure 58. Pressure contours ([22]).

Figure 59 shows the Mach number contours generated by the [22] algorithm. The low supersonic region formed behind the shock wave is well observed. It spreads around the blunt body surface. The shock wave behaves as expected, passing from

a normal shock wave, following oblique shock waves and finishing in Mach waves.

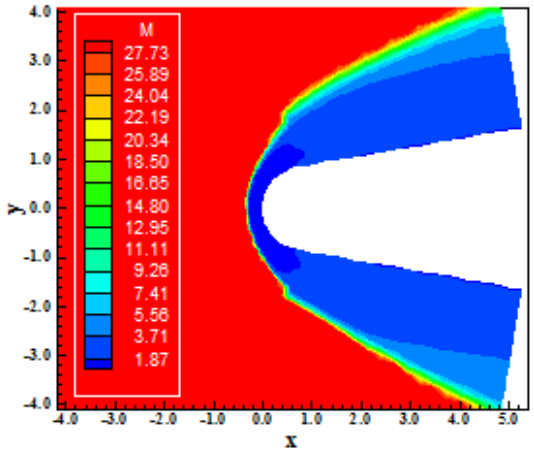

Figure 59. Mach number contours ([22]).

Figure 60 exhibits the translational/rotational temperature contours obtained by [22]. The temperature peaks reaches approximately 24,945 K and is centred at the body nose. Figure 61 shows the vibrational temperature contours, presenting good symmetry characteristics. The maximum vibrational temperature is 10,173 K and propagates around all geometry surface.

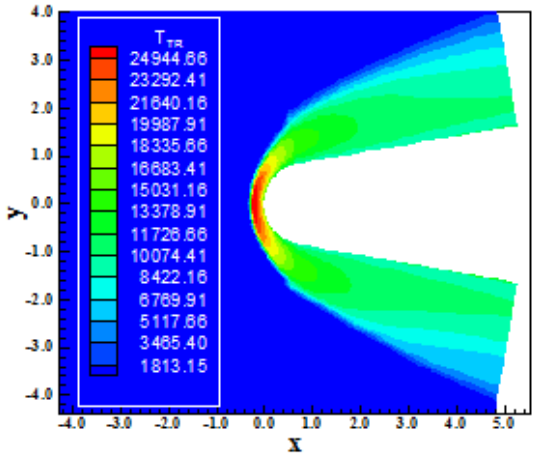

Figure 60. Translational/Rotational temperature contours ([22]).

Figure 62 presents the velocity vector field generated by the [22] scheme. The boundary layer has a very small thickness. The adherence and non-permeability conditions are well satisfied.

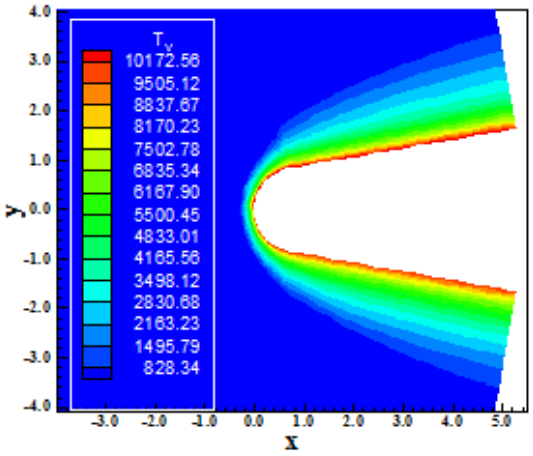

Figure 61. Vibrational temperature contours ([22]).

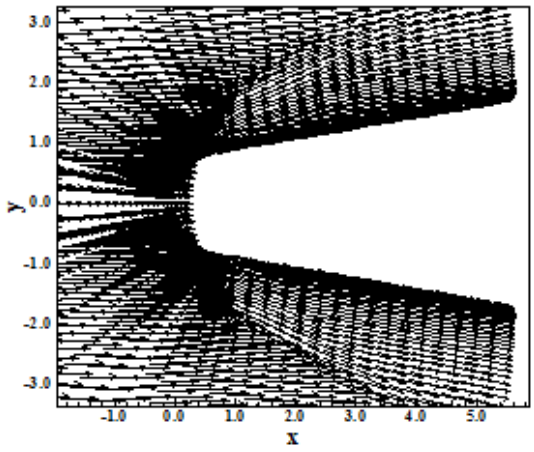

Figure 62. Velocity vector field.

10.1.7 Partial conclusions

As important conclusion from the blunt body results with the [2] and [22] numerical schemes, it is notable the most physical solutions obtained with the [22] scheme, which captured considerable dissociation of CO_2, with formation of CO and O, in all studied cases, as expected. So, in qualitative terms and considering structured solutions, the best behavior is attributed to the [22] scheme.

10.1.8 Lift and drag coefficients

In Table 10 are exhibited the lift and drag aerodynamic coefficients for all eight (8) structured cases studied in this work. As can be observed, the most accurate results is due to [2], first order in space, viscous case. The most severe drag coefficient is again due to [2], first order accurate, viscous case. In all cases, the zero value to the c_L coefficient, which is the correct value to a zero angle of attack blunt body problem, is satisfied.

Table 10. Aerodynamic coefficients of lift and drag.

Case	c_L	c_D
[2] – 1st – Inviscid	-4.325×10^{-15}	0.388
[22] – 1st – Inviscid	-4.778×10^{-14}	0.378
[2] – 1st - Viscous	9.198×10^{-18}	0.467
[22] – 1st – Viscous	-1.015×10^{-14}	0.428
[2] – 2nd - Inviscid	7.195×10^{-17}	0.385
[22] – 2nd – Inviscid	-2.963×10^{-14}	0.354
[2] – 2nd - Viscous	-3.839×10^{-17}	0.447
[22] – 2nd - Viscous	-3.335×10^{-15}	0.419

10.1.9 Computational data

The computational data of the present simulations are shown in Tab. 11. The best performance, converging in a minor number of iterations and wasting minor time, is due to the [22] scheme. The [22] scheme could also use the maximum CFL number by an explicit algorithm.

Table 11. Computational data.

Case	CFL	Iterations
[2] – 1st – Inviscid – S(1)	0.4	731
[22] – 1st – Inviscid – S	0.9	529
[2] – 1st – Viscous – S	0.2	3,964
[22] – 1st – Viscous – S	0.9	916
[2] – 2nd – Inviscid – S	0.2	1,589
[22] – 2nd – Inviscid – S	0.7	603
[2] – 2nd – Viscous – S	0.2	4,458
[22] – 2nd – Viscous – S	0.9	983
[22] – 1st – Inviscid – U(2)	0.6	572
[22] – 1st – Viscous – U	0.5	2,143

(1) S : Structured; (2) U : Unstructured.

11 Conclusions

This work, first part of this study, describes a numerical tool to perform thermochemical non-equilibrium simulations of reactive flow in two-dimensions. The [2] and [22] schemes, in their first- and second-order versions, are implemented to accomplish the numerical simulations. The Euler and Navier-Stokes equations, on a finite volume context and employing structured and unstructured spatial discretizations, are applied to solve the "hot gas" hypersonic flows around a blunt body, around a double ellipse, and around an entry capsule, in two-dimensions. The second-order version of the [2] and [22] schemes are obtained from a "MUSCL" extrapolation procedure (details in [3]) in a context of structured spatial discretization. In the unstructured context, only first-order solutions are obtained. The convergence process is accelerated to the steady state condition through a spatially variable time step procedure, which has proved effective gains in terms of computational acceleration (see [4-5]).

The reactive simulations involve a Mars atmosphere chemical model of nine species: N, O, N_2, O_2, NO, CO_2, C, CO, and CN. Fifty-three chemical reactions, involving dissociation and recombination, are simulated by the proposed model. The Arrhenius formula is employed to determine the reaction rates and the law of mass action is used to determine the source terms of each gas species equation.

The results have demonstrated that the most correct aerodynamic coefficient of lift in the entry blunt body problem is obtained by the [2] scheme with first-order accuracy, in a viscous formulation, to a reactive condition of thermochemical non-equilibrium. Moreover, the [22] scheme presents the best mass fraction profiles at the stagnation line, characterizing good formation of O and CO. The results obtained with the double ellipse and the entry capsule geometries are presented in [31].

12 Acknowledgments

The first author acknowledges the CNPq by the financial support conceded under the form of a DTI (Industrial Technological Development) scholarship no. 384681/2011-5. He also acknowledges the infra-structure of the ITA that allowed the realization of this work.

References:

[1] ESA, MARSNET – Assessment Study Report, *ESA Publication SCI* (91) 6, January, 1991.

[2] B. Van Leer, Flux-Vector Splitting for the Euler Equations, *Lecture Notes in Physics*. Springer Verlag, Berlin, Vol. 170, 1982, pp. 507-512.

[3] C. Hirsch, Numerical Computation of Internal and External Flows – Computational Methods for Inviscid and Viscous Flows. John Wiley & Sons Ltd, 691p, 1990.

[4] E. S. G. Maciel, Analysis of Convergence Acceleration Techniques Used in Unstructured Algorithms in the Solution of Aeronautical Problems – Part I, *Proceedings of the XVIII International Congress of Mechanical Engineering (XVIII COBEM)*, Ouro Preto, MG, Brazil, 2005. [CD-ROM]

[5] E. S. G. Maciel, Analysis of Convergence Acceleration Techniques Used in Unstructured

Algorithms in the Solution of Aerospace Problems – Part II, *Proceedings of the XII Brazilian Congress of Thermal Engineering and Sciences (XII ENCIT)*, Belo Horizonte, MG, Brazil, 2008. [CD-ROM]

[6] R. K. Prabhu, An Implementation of a Chemical and Thermal Nonequilibrium Flow Solver on Unstructured Meshes and Application to Blunt Bodies, *NASA CR-194967*, 1994.

[7] S. K. Saxena and M. T. Nair, An Improved Roe Scheme for Real Gas Flow, *AIAA Paper 2005-587*, 2005.

[8] J. Evans, W. L. Grose, and C. J. Schexnayder, Effects of Nonequilibrium Ablation Chemistry on Viking Radio Blackout, *AIAA Paper 73-0260*, 1973.

[9] C. Park, G. V. Candler, J. T. Howe, and R. L. Jaffe, Chemical-Kinetic Problems of Future NASA Missions, *AIAA Paper 91-0464*, 1991.

[10] Table of Recommended Rate Constants for Chemical Reactions Occurring in Combustion, *NSRDS-NBS 67*, April, 1980.

[11] G. F. Mitchell, and T. J. Deveau, Effects of a Shock on Diffuse Interstellar Cloud, J. Astrophysics, No. 266, 1983, pp. 646-661.

[12] F. G. Blottner, M. Johnson, and M. Ellis, Chemically Reacting Viscous Flow Program for Multi-Component Gas Mixtures, *SC-RR-70-754*, Sandia Laboratories, December, 1971.

[13] G. V. Candler, Computation of Thermochemical Non-Equilibrium Martian Atmospheric Entry Flows, *AIAA Paper 90-1695*, 1990.

[14] R. N. Gupta, K. P. Lee, J. N. Moss, and K. Sutton, Viscous Shock Layer Solutions with Coupled Radiation and Ablation Injection for Earth Entry, *AIAA Paper 90-1697*, 1990.

[15] C. R. Wilke, A Viscosity Equation for Gas Mixtures, J. Chem. Phys., Vol. 18, No. 4, 1950, p. 517.

[16] G. V. Candler, and R. W. MacCormack, The Computation of Hypersonic Ionized Flows in Chemical and Thermal Non-Equilibrium, *AIAA Paper 88-0511*, 1988.

[17] L. Landau, and E. Teller, Theory of Sound Dispersion, *Physikalische Zeitschrift Der Sowjetunion*, Vol. 10, 1936, pp. 34-43.

[18] R. Monti, D. Paterna, R. Savino, and A. Esposito, Experimental and Numerical Investigation on Martian Atmosphere Entry, *AIAA Paper 2001-0751*, 2001.

[19] R. C. Millikan and D. R. White, Systematics of Vibrational Relaxation, *The Journal of Chemical Physics*, Vol. 39, No. 12, 1963, pp. 3209-3213.

[20] A. F. P. Houwing, S. Nonaka, H. Mizuno, and K. Takayama, Effects of Vibrational Relaxation on Bow Shock Stand-off Distance for Nonequilibrium Flows, *AIAA Journal*, Vol. 38, No. 9, 2000, pp. 1760-1763.

[21] C. Park, Assessment of Two-Temperature Kinetic Model for Ionizing Air, *Journal of Thermophysics and Heat Transfer*, Vol. 3, No. 13, pp. 233-244, 1989.

[22] M. Liou, and C. J. Steffen Jr., A New Flux Splitting Scheme, *Journal of Computational Physics*, Vol. 107, 1993, pp. 23-39.

[23] R. Radespiel, and N. Kroll, Accurate Flux Vector Splitting for Shocks and Shear Layers, *Journal of Computational Physics*, Vol. 121, 1995, pp. 66-78.

[24] L. N. Long, M. M. S. Khan, and H. T. Sharp, Massively Parallel Three-Dimensional Euler / Navier-Stokes Method, *AIAA Journal*, Vol. 29, No. 5, 1991, pp. 657-666.

[25] B. Van Leer, Towards the Ultimate Conservative Difference Scheme. II. Monotonicity and Conservation Combined in a Second-Order Scheme, *Journal of Computational Physics*, Vol. 14, 1974, pp. 361-370.

[26] P. L. Roe, In *Proceedings of the AMS-SIAM Summer Seminar on Large-Scale Computation in Fluid Mechanics*, Edited by B. E. Engquist et al, *Lectures in Applied Mathematics*, Vol. 22, 1983, p. 163.

[27] E. S. G. Maciel, and A. P. Pimenta, Thermochemical Non-Equilibrium Reentry Flows in Two-Dimensions – Part I, *WSEAS TRANSACTIONS ON MATHEMATICS*, Vol. 11, Issue 6, June, 2012, pp. 520-545.

[28] E. S. G. Maciel, Simulação Numérica de Escoamentos Supersônicos e Hipersônicos Utilizando Técnicas de Dinâmica dos Fluidos Computacional, *Doctoral Thesis*, ITA, CTA, São José dos Campos, SP, Brazil, 258p, 2002.

[29] R. D. Kay, and M. P. Netterfield, Thermochemical Non-Equilibrium Computations for a Mars Entry Vehicle, *AIAA Paper 93-2841*, July, 1993.

[30] NASA, Models of Mars' Atmosphere [1974], *NASA SP-8010*.

[31] E. S. G. Maciel, and A. P. Pimenta, Thermochemical Non-Equilibrium Entry Flows in Mars in Two-Dimensions – Part II, to be submitted to *WSEAS TRANSACTIONS ON APPLIED AND THEORETICAL MECHANICS*.